Transcriptional impacts of substance use disorder and HIV on human ventral midbrain neurons and microglia

Alyssa M. Wilson[1,2,*], Michelle M. Jacobs[1], Tova Y. Lambert[2,†], Aditi Valada[2,†], Gregory Meloni[1], Evan Gilmore[1], Jacinta Murray[1], Susan Morgello[1,3,4,‡], Schahram Akbarian[2,3,5,‡]

[1]Department of Neurology, Icahn School of Medicine at Mount Sinai, New York, NY 10029, USA.
[2]Department of Psychiatry, Icahn School of Medicine at Mount Sinai, New York, NY 10029, USA.
[3]Department of Neuroscience, Icahn School of Medicine at Mount Sinai, New York, NY 10029, USA.
[4]Department of Pathology, Molecular and Cell Based Medicine, Icahn School of Medicine at Mount Sinai, New York, NY 10029, USA.
[5]Department of Genetics and Genomic Sciences, Icahn School of Medicine at Mount Sinai, New York, NY 10029, USA.
[†]Present address: Albert Einstein College of Medicine, New York, New York 10461, USA.
[‡]These authors contributed equally to this work.

[*]Email: alyssa.wilson@mssm.edu

Abstract

For people with HIV (PWH), substance use disorders (SUDs) are a prominent neurological risk factor, and the impacts of both on dopaminergic pathways are a potential point of deleterious convergence. Here, we profile, at single nucleus resolution, the substantia nigra (SN) transcriptomes of 90 postmortem donors in the context of chronic HIV and opioid/cocaine SUD, including 67 prospectively characterized PWH. We report altered microglial expression for hundreds of pro- and anti-inflammatory regulators attributable to HIV, and separately, to SUD. Stepwise, progressive microglial dysregulation, coupled to altered SN dopaminergic and GABAergic signaling, was associated with SUD/HIV dual diagnosis and further with lack of viral suppression in blood. In virologically suppressed donors, SUD comorbidity was associated with microglial transcriptional changes permissive for HIV infection. We report HIV-related downregulation of monoamine reuptake transporters specifically in dopaminergic neurons regardless of SUD status or viral load, and additional transcriptional signatures consistent with selective vulnerability of SN dopamine neurons.

Introduction

The HIV pandemic continues to pose a global health burden, despite considerable advances in treatment and prevention[1,2]. Although a large fraction of people with HIV (PWH) are receiving life-saving antiretroviral therapy (ART), treatment does not eradicate the virus, and HIV persists in multiple tissue reservoirs including the brain. PWH may develop neurologic disorders that are predicated in part on immune dysfunction, and that are presumed to result from the action of HIV on nervous system cells[2–4]. An important co-morbidity relevant to HIV neurologic disease is substance use disorder (SUD), and in particular injection drug use[5], with its negative impact on health by a multitude of factors including risky behaviors, emergence of medical and psychiatric sequelae, and lack of compliance with therapy[6–15]. Notably, HIV and SUD show a striking neuroanatomical convergence on dopamine-rich structures in brain. In ventral midbrain[16] this

includes substantia nigra (SN)[17,18], a region important for mediating habitual behaviors and salience of cues associated with drug use[18], withdrawal-related anhedonia and dysphoria, and extra-pyramidal motor dysfunction[19,20]. There is also evidence, mostly from preclinical work, that drug-of-abuse-induced dynamic adaptations in addiction-relevant dopaminergic circuitry could worsen HIV-associated cognitive and behavioral deficits[21], with multiple dopaminergic signaling pathways converging on susceptible myeloid cells to promote viral entry and replication[22,23].

Despite its importance, very little is known about cellular and molecular alterations in the ventral midbrain of PWH with or without SUD comorbidity, with the majority of studies limited to quantification of neurotransmitter (e.g., dopamine) in bulk tissue or neuroimaging and analysis of cerebrospinal fluid (CSF) in the context of advanced disease (AIDS)[24–26]. Herein, we profile for the first time, the ventral midbrain transcriptomes from n=90 total PWH and people without HIV ("HIV-"), at single (cell) nucleus resolution, and deliver first insights into the cell-type-specific neurogenomic responses to chronic infection and SUD. We specifically examine responses to opioid and/or cocaine SUDs, given the high prevalence of these substances and their combination among PWH[27–29]. Our analyses, focused on SN dopaminergic (DA) and GABAergic (GABA) neurons and their surrounding microglia, strongly suggest that SUD for opioids and cocaine creates, even in donors with antiretroviral therapy (ART)-mediated viral suppression, a molecular environment permissive for HIV viral replication and risk for cytotoxic damage to dopaminergic neurons. In addition, we report a stepwise progression of transcriptomic dysregulation for opioid/cocaine SUD and HIV comorbidity that culminates in widespread neuronal pathology and pronounced inflammatory signatures in microglia from individuals without viral suppression (viremia) in the context of SUD.

Results

SN cell type composition in the context of HIV and SUD

We dissected ventral midbrain for unilateral collection of the SN including *pars compacta* and *pars reticulata* from n=90 donors collected by the Manhattan HIV Brain Bank (MHBB) (39 female/ 51 male; mean+/-standard deviation age 54.0+/-11.4 years; 33% Hispanic, 38% non-Hispanic Black, 22% non-Hispanic White; Table 1), including 67 participants followed longitudinally in the MHBB with deep clinical phenotyping during years of study participation (median 6, maximum 21 years). We assigned each donor to one of three HIV statuses: negative ("HIV-", n=28 donors), HIV positive with "undetectable" final plasma viral load (VL) defined as <50 RNA copies/mL ("HIV+u", n=30 donors), or HIV positive with viremia, evidenced by a detectable final plasma VL ("HIV+d", n=32 donors [viral RNA copies/mL range 65 to >750,000, median 6,721]). We further grouped donors by substance use into "SUD-" or "SUD+" for any combination of opioid/cocaine SUD (n=60 SUD+, including n=42 with a history of misusing opioids, of which n=28 had a history of misusing both opioids and cocaine). This grouping produced HIV-/SUD-defined subgroups that were overall closely matched with regard to demographic factors: SUD-HIV- (n= 13); SUD+HIV- (n=15); SUD-HIV+u (n=10); SUD+HIV+u (n=20); SUD-HIV+d (n=7); and SUD+HIV+d (n=25) (Fig. 1A, Tables S1-S3). Notably, the wider MHBB cohort from which these donors were selected had a high prevalence of polysubstance SUD, with approximately three quarters of SUD-positive individuals endorsing symptoms for two or more drug classes.

We processed nuclei in pools of up to 4 donors, with most pools containing mixed HIV/SUD donor phenotypes, using the 10x Chromium 3' system followed by Illumina sequencing. We then matched each single, sequenced nucleus to a specific donor using SNP-array genotyping and demuxlet[30], and applied a series of quality control (QC) filters to each nucleus (Figs. S1A-C),

including an upper threshold on the proportion of mitochondrial reads (set at 0.0128; Fig. S1A). We note that 100% of glial and 98% of neuronal nuclei that passed QC had a minimum of 200 genes expressed (Figs. S1B, C), thereby exceeding standards from published SN reference sets[31,32] (compare Figs. S2A and S2B). After preprocessing, the final dataset amounted to a total of 200,732 QC-passing nuclei, with 81/90 donors contributing >1,000 nuclei (Fig. S1D; Table S4; Methods).

We first asked whether SN cell type composition is affected in the context of HIV and SUD. To maximize sensitivity for potential shifts in cellular subpopulations, we used as input 20,000/36,601 gene transcripts (Fig. S1E) as opposed to more typically suggested sizes of ~2,000[33], and we performed a likelihood-based, agnostic approach for cell typing (Methods). Our approach produced 12 major cell types (Figs. 1B, C, Fig. S3) that by numbers and proportions closely matched those reported for human SN single-cell-based transcriptomic reference sets[34,35], with the largest share (65%) composed of oligodendrocytes and their precursors, and 14-15% made up of microglia and astrocytes. In contrast, SN neurons, endothelium, lymphocytes and macrophages each contributed a much smaller proportion of nuclei. There were no significant differences for 176/180 statistical comparisons of cell type proportions across HIV/SUD donor groups, indicating that the overall representation of major cell types in SN is preserved independent of HIV or SUD status (Figs. 1D, E; Table S5).

Cell-specific transcriptomic responses to HIV infection show progression in the context of SUD, as well as SUD-independent downregulation of monoamine transporters in DA neurons

To examine cell-level impacts on SN function due to SUD, HIV, or both, we performed differential expression analysis (DEA; Methods) by stratifying the entire cohort of n=90 SN samples first by HIV groupings to interrogate effects of SUD, thereby comparing SUD+ vs. SUD- for HIV- donors, SUD+ vs. SUD- for HIV+u donors, and SUD+ vs. SUD- for HIV+d donors (Fig. 2). Likewise, to examine the impacts of HIV status, we stratified by SUD grouping, comparing HIV+u vs. HIV- for SUD+ donors, then for SUD- donors, and repeating similar analyses for HIV+d vs. HIV- and HIV+d vs. HIV+u, first for SUD+ and then for SUD- donors (Figs. 3-5).

We focused our DEAs on SN DA neurons and GABA neurons, given their key role in addiction circuitry and potential sensitivity to HIV infection[25,36–39], and also on microglia, as mediators of neuroinflammation and host cells for HIV genomic integration[39–41]. We reduced the rate of false-positive differentially expressed genes (DEGs) using multiple steps. First, we applied cross-fold validation (k=3 folds), creating for each comparison and cell type three separate subsets of nuclei, performing DEA on each, and retaining only DEGs appearing in all 3 subsets. Second, we applied DESeq2 DEA model fitting, to exclude genes with low expression dispersion estimates and low counts[42,43] (Methods).

Using the above DEA pipeline on DA neurons, and stratifying for HIV status (to assess the impact of SUD), we called 51 genes downregulated in SUD+HIV- vs. SUD-HIV- donors (false discovery rate [FDR] $p<0.05$; log2 fold change [l2fc] > variable values, dependent upon FDR, sample size, and dataset information content[43]; Data S1). These DEGs enriched gene ontology (GO) terms[44] linked to neuronal function, including axon myelination, presynaptic organization, cell adhesion, and Na^+ transport (Fig. 2A; Data S2). Notably, SUD+HIV+u donors, while exhibiting significant sharing of these downregulated DEGs with SUD+HIV- donors (by permutation test, $p<10^{-5}$) also showed 82 uniquely upregulated DEGs, which enriched most prominently GO terms for axon growth and presynaptic transmission (Fig. 2B, J, K; Data S2). This observation suggests enhanced sensitivity to SUD in the context of HIV comorbidity, even in

150 the face of viral suppression (for HIV+u donors). In contrast, SUD+HIV+d had 0 DEGs vs. SUD-
151 HIV+d (Figs. 2C, P; Data S1), suggesting that for these two viremic donor groups, transcriptomic
152 alterations of SN DA neurons were primarily driven by factors related to active HIV replication
153 (viremia).
154
155 Indeed, this is what we observed when the DEA of DA neurons was stratified for SUD status (to
156 assess the impacts of HIV), with SUD+HIV+d donors having 40 up-/ 38 down- regulated DEGs
157 vs. SUD+HIV- (Fig. 3B). Furthermore, while downregulated DEGs were highly shared between
158 SUD+HIV+d and SUD+HIV+u donors (35 shared, $p<10^{-5}$; Figs. 3A, B), many viremia-specific
159 (HIV+d) effects were identified (56 downregulated and 5 upregulated DEGs that enriched
160 different GO terms; Fig. 3C, Data S2). Importantly, the presence of SUD increased virus-
161 associated transcriptomic dysregulation: DA neurons from SUD-HIV+d and SUD-HIV+u donors
162 consistently showed a much smaller number of DEGs than their SUD+ counterparts (by
163 approximately 1/3; Figs. 3D, E) and in the absence of SUD, HIV+u and HIV+d transcriptomes
164 were indistinguishable (n DEGs = 0, Fig. 3F).
165
166 Despite the above SUD-attributable differences, a striking commonality in all HIV+ groupings
167 also emerged from our analyses: DA neurons from all HIV+ groups, regardless of SUD status or
168 VL, showed significant downregulation in *SLC6A3* dopamine and *SLC18A2* monoamine
169 transporter genes (Figs. 3A, B, D, E; Data S1, S2), together with a more variable dysregulation of
170 genes related to neuronal immune responses, presynaptic vesicle release, synaptic signaling, and
171 cell-cell adhesion. From all the above observations, we draw two conclusions. First, the
172 neurogenomic response to HIV infection, both for donors with viral suppression and without,
173 alters fundamental signaling mechanisms in SN DA neurons including dopamine reuptake.
174 Second, SUD comorbidity enhances abnormality in HIV+ donors, driving a stepwise progression
175 in DA neuron dysregulation, in which abnormalities are more severe in SUD+ compared to SUD-
176 donors and enhance the effects of systemic viral replication (Figs. 3C, F).
177
178 Next, we ran our DEA pipeline on SN GABA neurons, which produced few DEGs across all
179 comparisons (there were median [interquartile range or IQR] 0 [0, 0.75] GABA DEGs for each of
180 our 6 DEAs, as opposed to 24 [0, 40.75] DA DEGs; compare Figs. 2A-C to D-F and Fig. 3 to Fig.
181 4). Stratification by HIV status produced only one DEG attributable to SUD: downregulation of
182 *RBFOX1* GABAergic transcription factor in SUD+HIV+u vs. SUD-HIV+u donors (associated
183 with decreased inhibition[45,46]; Figs. 2D-F, L, M). However, stratification by SUD revealed severe
184 HIV-associated GABA neuron transcriptomic dysregulation in viremic (HIV+d) donors with
185 SUD, pointing to reduced inhibitory neurotransmission (Figs. 4B, C; Data S2). We counted 115
186 HIV-associated DEGs (96 down, 17 up) in SUD+HIV+d donors vs. SUD+HIV-, and 322 DEGs
187 (266 down, 57 up) in SUD+HIV+d vs. SUD+HIV+u donors. There was significant overlap ($p <$
188 10^{-5}) between these two comparisons, including downregulated DEGs involved in GABA
189 production, glutamatergic G-protein-coupled receptor (GPCR) signaling, homophilic cell-cell
190 adhesion, and action-potential-associated membrane depolarization (Data S1, S2). In addition,
191 there was downregulation of several opioid-related transcripts, including of postsynaptic opioid-
192 binding cell adhesion molecule (OBCAM) *OPCML*, which is downregulated during chronic
193 opioid agonist exposure[47–49]; the closely related neurotrimin (*NTM*); ephrin-B1 receptor (*EPHB1*),
194 which colocalizes and interacts closely with ephrin-B2 receptor[50,51] as a mediator of *OPCML*
195 signaling[49]; and non-coding RNA *AC073225.1*, previously reported to show decreased expression
196 in opioid use disorder (OUD)[52]. These alterations were specific to SUD+HIV+d, given that SUD-
197 HIV+d vs. SUD-HIV-, SUD-HIV+u vs. SUD-HIV-, and SUD+HIV+u vs. SUD+HIV-
198 comparisons completely lacked significant differences in gene expression (n DEGs = 0).
199

Finally, we applied our stratified DEA pipeline to SN microglia, resulting in hundreds of DEGs attributable to SUD (Figs. 2G-I, N, O, Q). These transcriptional alterations were mostly enriched for various combinations of pro- and anti-inflammatory molecules (Data S1, S2), in broad agreement with recent studies that have reported upregulation of immune signaling genes and transcriptomic signatures indicative of microglial activation and altered glial motility in OUD, chronic opioid exposures, and overdose[34,53–55]. However, in our analysis a substantial fraction of SUD-attributable microglial DEGs were unique to each HIV grouping (Figs. 2N, O), pointing to distinct microglial responses to SUD in the context of varying levels of HIV (HIV-, HIV+u, HIV+d[56]). For example, SUD-associated gene sets supporting reduced protein stabilization and interferon-1 production were seen only in HIV+d, and not in the other HIV groupings (Data S2).

Stratifying by SUD groupings (Fig. 5), we also counted hundreds of microglial DEGs attributable to HIV, including 446 down- and 89 up-regulated DEGs for SUD- subjects with viral suppression (SUD-HIV+u) vs. HIV- controls (SUD-HIV-), >50% of which were replicated in viremic SUD-HIV+d donors ($p < 10^{-5}$). These shared changes primarily involved gene sets for increased inflammatory signaling, decreased phagocytosis and iron ion responses, and increased stress response protein folding/refolding (Data S2). For the SUD-HIV+d group, there were additional changes vs. SUD-HIV+u, including enhancements of immune signaling and telomere maintenance/remyelination processes, as well as antiviral-response-related reductions in glucose transport/GPCR signaling[57,58]. In the context of SUD (Figs. 5A-C), when comparing SUD+HIV+u and SUD+HIV+d donors to SUD+HIV- controls, microglial transcriptional alterations included multiple gene sets related to immune activation, many of which were shared; further, some of these shared effects were opposite to shared HIV effects in the absence of SUD. For example, in the absence of SUD, HIV resulted in downregulated iron ion responses; in the context of SUD, iron ion responses were upregulated (Data S2). Additionally, in the context of SUD, microglia-mediated regulation of synaptic signaling was dysregulated in both HIV+u and HIV+d donors; this effect was absent in the SUD- comparisons.

Coordinated DEG clusters link microglial and neuronal function, and highlight microglial changes in SUD+HIV+u donors supportive for HIV replication

Next, we wanted to complement our pathway-by-cell type analyses with an alternative approach, by capturing DEGs with statistically linked, or "coordinated", expression levels across the majority of donors within an SUD/HIV group. To that end, for each DEA we performed, we searched for groups of DEGs that had a high degree of inter-patient covariance (Methods). We selected similarity-based DEG subclusters with average pairwise similarity scores >0.75, our cutoff for identifying gene groups with the most ubiquitous coordinated transcriptional alteration (Fig. 6A), for functional annotation. In the following, we discuss these DEG subclusters, with a focus on microglia-neuron biological functions and interactions.

We first examined highly coordinated DEGs for DA neurons and microglia, using the 4 DEAs that showed changes for either SUD, suppressed HIV (HIV+u), or both (Fig. 6B). We identified 117 highly coordinated DEG subclusters (with median [IQR] 10 [6,21] DEGs per subcluster; Table S6, Data S4). Interestingly, 17 of these subclusters contained a mix of DA and microglial DEGs, suggesting DA-microglial interactions. Two of the 17 were specific for the comparison of SUD+HIV- vs. SUD-HIV- (related to impacts of SUD in the absence of HIV; Figs. 6D-G). Both of these subclusters involved glycoproteins: one (C22S1) linked decreased N-glycan synthetic enzyme *FUT8* fucosyltransferase[59] in both microglia and DA neurons to altered DA neurotransmission (reduced membrane maintenance, reduced pre-/ post-synaptic machinery, slowed presynaptic release, and increased excitability; Figs. 6D, E). Notably, *FUT8* has previously been associated with increased basal microglial reactivity[60] and impaired neuronal

membrane maintenance[61–63]. The other subcluster (C22S2) linked decreased DA neuron expression of *GPM6B* glycoprotein to a microglial switch from oxidative phosphorylation to aerobic glycolysis[64,65], as well as to deficits in the microglial antiviral response and in transcripts associated with increased microglial-neuroligin-1-mediated excitatory synapse formation (*MDGA2*↓[66,67]) and increased catecholaminergic receptor responses (*SPATS2L*↓[68,69]), among others (Figs. 6F, G).

For dual-diagnosis (SUD+HIV+u) donors, there were 9 mixed DA neuron/microglial subclusters. Three of these closely resembled the subclusters described above for SUD without HIV, specifically for DA DEGs (see "SUD conserved impacts," denoted by deep pink color, in Figs. 6B, D, F; Data S4). Additionally, and remarkably as these were virally suppressed donors, 5 out of 9 had prominent representation of DEGs linked to HIV infection and replication (Data S4). For example (subcluster C16S2, Figs. 7C, D), DA upregulation of the Na+-Ca2+ exchanger *SLC8A1* was linked to 31 microglial DEGs important for HIV transcription and replication (*HIF1A*↑[70,71], *HIF1A-AS3*↑[72–74], *HIVEP2*↑[75–78], *SYTL3*↑[79,80], *REL*↑[81–84], *ELL2*↑[85,86]), HIV host entry and genome stabilization (*TFRC*↑[87], *SEC14L1*↑[88], *CD55*↑[89,90]) or viral stabilization (*SIPA1L1*↑ or *E6TP1*↑[91]), and HIV-1 intracellular compartment release (*ATP1B3*↑[92]). We note that Na+Ca2+-exchanger-mediated prolonged neuronal excitation was previously linked to HIV infection in an *in vitro* model[93]. Thus, these subclusters indicated that in virally suppressed PWH, SUD may result in microglial changes permissive for HIV. Other DEG subclusters for SUD+HIV+u donors also linked microglial dysregulation to increased excitability in DA neurons (Figs. 7G, H; Data S4).

Another specific SUD+HIV+u subcluster (subcluster C17S0, Figs. 7E, F) linked microglial upregulation of receptors for neurodegeneration-associated inflammatory phagocytosis (*OLR1*[94,95], and *ITGAX*, which targets complement-coated particles[96]) to DA neuronal downregulation of neuronal maintenance genes *CLMN*[97,98] and *PEX5L*[99]). Taken together, this subcluster suggests that for individuals with undetectable HIV, SUD+/HIV+u synergy still may be associated with damage to vulnerable DA neuron populations.

In SUD+HIV+d, impaired GABAergic function is coordinated with increased microglial pro-inflammatory signaling

We also identified DEG subclusters for GABA neurons and microglial cells, to explore their relationships in SUD+HIV+d, because in our DEAs this subgroup specifically showed signs of disrupted GABA neuron function (Figs. 4B, C; Data S4). Compared to SUD+HIV+u, SUD+HIV+d individuals had microglial upregulation of DEGs linked to pro-inflammatory signaling (*EPSTI1*[100], *IFI44L*[101,102]) together with alterations in GABAergic regulators of aging (*RANBP17*↓[103]), cellular maintenance, GABAergic transmission (*SYT9*↓[104]; *DDAH1*↓[105]), and ER-Ca2+-mediated apoptosis (*DPP10*↑, *RYR3*↑[106,107]). Therefore, the impairment of GABAergic regulation in SUD+HIV+d is linked to pro-inflammatory responses in microglia.

Discussion

We have explored cell-type-specific transcriptional changes in the SN of donors with HIV, opioid/cocaine SUD, or both. Our rationale for HIV groupings (HIV-, HIV+u, HIV+d) was based on an extant literature that has linked plasma HIV to brain microglial activation and other aspects of brain pathology[108], and on the relevance of plasma HIV load as a standard for guiding patient care. Our rationale for using a polysubstance (opioid/cocaine) approach to SUD groupings was based on the pronounced polysubstance prevalence both in the MHBB cohort and overall in the United States[109], the importance of these particular drug classes to the HIV epidemic in New York

City[27–29], and a call in existing literature for more research on polysubstance users, which reflects the lifetime exposures of the majority of individuals with chronic SUDs[109–111].

Our findings, summarized in Fig. 8, demonstrated altered expression of hundreds of pro- and anti-inflammatory transcripts in microglia attributable both to SUD and HIV, with the combined effects of SUD and HIV resulting in a more pronounced dysregulation of the microglial inflammatory transcriptome, particularly in those donors lacking viral suppression (HIV+d). These changes were significantly coupled with abnormalities in neuronal integrity, excitability, and neurotransmission. Perhaps most strikingly, we observed that dysregulated DA neuron transcription in the SN of virally suppressed, opioid/cocaine-SUD+ HIV+u donors was linked to upregulated microglial transcription of genes permissive for HIV infection, replication, and reactivation, along with an altered microglial antiviral response and increased neurodegeneration-associated inflammatory phagocytosis (Data S4). These findings, in a carefully phenotyped, prospectively characterized human population, are striking given the previously reported evidence of a selectively expanded brain viral reservoir in ART-treated, Simian Immunodeficiency Virus (SIV)-infected non-human primates with chronic morphine exposure[112,113]. In this SIV model, reservoir expansion occurred in conjunction with microglial transcriptional changes indicative of immunosuppression and degeneration, relative to SIV+ opioid-negative comparators[112,113]. With the techniques utilized in the present study, we are unable to comment on the brain viral reservoir in our donors, and we identified only 2 HIV transcripts in our entire collection of nuclei (Methods). This is not surprising, given that in a previous study with similar snRNA-seq methodology, HIV transcripts in a subset of microglial nuclei were limited to donor brains displaying the histopathology of active brain viral replication or HIV encephalitis (HIVE)[114]. None of the donors in our present study had histopathologic evidence of HIVE, assessed as part of the standard MHBB neuropathology protocol[115,116]. The lack of viral transcript detection constitutes a limitation of our present work. Furthermore, it contrasts with recent study in which HIV RNA was detected in whole-cell, sorted brain microglia from 2 of 3 virally suppressed HIV+ donors[117,118]. The donors in this prior study were exclusively male and described as having been on ART "until at least 2 wk before death"[117]. The discrepancy between our study and this previous study warrants further investigation, and it could reflect differences in nuclear vs. cytoplasmic substrates for analysis; the time at which ART therapy was discontinued in donors prior to death; or possibly either geographical variabilities in circulating and evolving HIV strains or differing genetic determinants of immune function and viral control in donor populations.

Another important aspect of our work was the demonstration that SUD comorbidity in the context of HIV status exerted impacts on SN neuronal transcriptomes in a stepwise progression. In HIV-donors, we observed only downregulation of DA neuronal transcripts that potentially induce impaired function, senescence-like changes, and increased excitability (Fig. 6, Data S4). In virally suppressed individuals (HIV+u), we observed both a shared (with HIV-) downregulation of DA neuronal genes potentially increasing DA neuron excitability, as well as uniquely upregulated DEGs that suggested enhanced sensitivity to SUD (Fig. 2). Similarly, we observed evidence of enhanced sensitivity to HIV in SUD+HIV+u donors (Fig. 3). With viremia/absence of viral suppression (HIV+d), we further observed changes affecting hundreds of GABAergic transcripts and potentially compromising inhibitory neurotransmission. As microglial transcriptional dysregulation had unique components and also progressed with each HIV grouping, this raises the question of what drives progression, and whether it is unidirectional (driven by one cell type) or bidirectional (driven reciprocally). Recent work in mixed cell cultures (containing microglia with either DA or GABA neurons) has shown that healthy neurons may drive HIV into latency in microglia; and conversely, neuronal damage, including substance-related damage, fosters microglial HIV reactivation and viral expression, thereby further compromising neuronal health

349 due to enhanced microglia-mediated neurotoxicity[119]. Our findings in postmortem human brain
350 raise the possibility that similar bidirectional phenomena may be relevant in human, but future
351 studies will be needed to further examine the mechanisms driving neuronal and glial dysfunction,
352 expanding on our observations of transcriptomic signatures of coordinated detrimental
353 interactions between HIV and SUD (for a more complete listing of significant coordinated
354 abnormalities, see Data S3, S4).
355
356 Finally, while we have focused on effects of HIV and SUD comorbidity in altering SN neuronal
357 and microglial transcriptomes, it is noteworthy that in all our HIV+ donor groups, regardless of
358 viral load or SUD status, DA neurons showed a consistent deficit in the expression of the
359 dopamine and monoamine reuptake transporters *SLC6A3* (encoding the protein "DAT") and
360 *SLC18A2*, respectively, two key regulators of DA turnover at synapses. Combination cocaine-
361 and-raclopride positron emission tomography (PET) studies of viremic PWH, both with and
362 without SUD, have demonstrated similar abnormalities at the protein level *in vivo*, showing
363 decreased DAT signal in the dopamine-terminal-rich basal ganglia[120,121]. The prevailing
364 hypothesis for this phenomenon was that HIV viral proteins, including its transactivator of
365 transcription or Tat and others, directly bind to monoamine transporters, thereby inhibiting
366 monoamine (including dopamine) reuptake and damaging DA neurons[122,123]. However,
367 downregulation of DAT and monoamine reuptake transporter transcripts occurred in our study
368 even in the virally suppressed HIV+ SUD- donor group; and furthermore, evidence of viral Tat
369 transcripts in our brains was lacking. The DA-neuron-specific RNA results presented here point
370 to a transcriptional mechanism resulting in decreased monoamine transporter expression that,
371 while linked to some unified aspect of HIV infection, does not require evidence of ongoing viral
372 replication or transcription.
373
374 In summary, the strengths of our study include: a large number of carefully phenotyped brain
375 donors with large amounts of prospectively collected data on SUD and immunovirologic status;
376 novel analytic pipelines that are tolerant to abnormality yet rigidly subjected to quality
377 assurance/QC procedures that exceed other published norms; analytic groups parsed by clinically
378 relevant factors in HIV and SUD; and in-depth annotation of DEG groups that show coordinated
379 expression in most members of their associated donor group (Data S3, S4). Limitations include a
380 lack of viral transcript detection and the lack of mechanistic exploration of the multiple
381 transcriptomic abnormalities described in these donor groupings. Future studies are indicated to
382 further understand the significance of these genomic adaptations for future development of
383 therapies for PWH and SUD.
384
385
386 **Methods**
387 ***Brain donor tissue and clinical data collection***
388 Brain donors were autopsied and their donations curated by the MHBB between the years 1999
389 and 2021, using study protocols and consent documents approved by the Icahn School of
390 Medicine at Mount Sinai (ISMMS) Institutional Review Board (IRB; IRB Approval Number
391 STUDY-11-00388). Briefly, at the time of autopsy, the entire brain was removed, photographed,
392 and bisected, and one hemisphere was placed in phosphate-buffered formalin for subsequent
393 processing, gross neuropathologic review, sectioning, and histological analysis[115]. The other
394 hemisphere was immediately sectioned, each section photographed, and then was snap-frozen
395 between aluminum plates chilled to a temperature of -85° Celsius (C). Frozen brain sections were
396 stored at -85°C in a monitored facility. For this study, samples of ventral midbrain containing
397 recognizable pigmentation indicative of SN were dissected, using a rotary saw on a cold table
398 (chilled to -20°C). As there was some rostro-caudal variation in the anatomical level at which

399 each donor's SN was dissected, we accounted for the relative location as rostral midbrain (SN at
400 the transverse level of the red nucleus) or caudal midbrain (at the level of the cerebellar
401 peduncular decussation) and included this as a covariate in our differential expression analysis
402 (see below).
403
404 Prospectively collected clinical information was available for 67 donors (62 HIV+, 5 HIV-) as a
405 consequence of their participation in the MHBB longitudinal, observational study. For 23 other
406 HIV- donors, information was extracted by medical record review at the time of demise.
407 Substance use characterization (DSM IV dependency diagnoses) for those followed in the MHBB
408 study was obtained with either the Psychiatric Research Interview for Substance and Mental
409 Disorders (PRISM) versions 1.9b and SL[124] or the World Health Organization Composite
410 International Diagnostic Interview (CIDI) version 2.1[125], and drug utilization was monitored by
411 urine toxicologic analysis for opiates, cocaine, and other psychoactive substances at each study
412 visit, as described previously[126]. At the time of urine toxicology, the donor's reported medications
413 were examined to determine whether psychoactive substances were prescribed secondary to
414 medical illness. For donors not enrolled in the prospective MHBB study, DSM IV diagnoses and
415 problematic utilization were obtained from medical records, inclusive of urine toxicologic
416 analysis when available. Immunovirologic data (CD4 T-cell counts and plasma HIV VL) were
417 similarly obtained either as a prospective research study laboratory or retrospectively extracted
418 from medical records; all were performed in the CLIA-certified laboratories of the Mount Sinai
419 Hospital. In this study, for HIV+ individuals, we used a VL of 50 copies/mL as the threshold for
420 HIV detectability, to be consistent with the quantitative lower limit of the earliest assays utilized
421 in the MHBB cohort.
422
423 ***snRNA-seq***
424 We performed sample processing consisting of nuclei purification, RNA extraction, and
425 subsequent generation of snRNA-seq libraries, following almost exactly a previously described
426 method[34] for sequencing of pooled tissue samples. Briefly, we homogenized tissue aliquots
427 containing pooled ventral midbrain from SN using a douncer in a mixture of lysis buffer and
428 RNase inhibitor. In each library, we pooled tissue from 1 to 4 unique donors to increase
429 sequencing throughput; we also added a small volume of mouse tissue to most libraries (28/33) as
430 a negative control to create a threshold for spurious HIV reads (for future work). On pooled
431 tissue, we used a lysis and sucrose buffer gradient to isolate nuclei during ultracentrifugation. We
432 resuspended nuclei in a BSA solution containing RNase inhibitor, stained them with DAPI
433 nucleophilic dye, and used fluorescence-activated nuclei sorting (FANS) to collect 300,000
434 DAPI+ nuclei for input into the 10x Chromium NEXT GEM Single 3' v3.1 (Dual Index) Protocol
435 according to manufacturer instructions. We quantified libraries using qPCR prior to sequencing
436 on the Illumina NovaSeq platform. Sequencing was performed by the New York Genome Center.
437 As described below, each library was separated by donor after sequencing and prior to analysis,
438 using genotype-based demultiplexing, such that we performed our analyses on a per-donor basis
439 (see below).
440
441 We generated the first round of snRNA-seq libraries by pooling tissue from 3 to 4 patients per
442 library, then performed QC and generated additional snRNA-seq libraries for donors with <1,000
443 QC-passing nuclei, in each pooling tissue from only 1 to 2 patients to increase the per-patient
444 nuclear yield. We added libraries for low-yield donors until the tissue sample was exhausted or
445 the total number of quality-passing nuclei exceeded 1,000 for 90% of donors, resulting in a total
446 of 51 libraries across the 90 study donors. We determined the threshold of 1,000 QC-passing
447 nuclei per donor using a power analysis (see below).
448

449 ***Imputed donor SNP arrays for demultiplexing***
450 We used donor SNP arrays as a reference to demultiplex pooled snRNA-seq data, generating
451 them from donor cerebellum tissue using the Illumina Infinium Global Screening Array platform
452 (GSA-24v3.0). We prepared DNA for each donor at a final concentration of 20 ng/µL.
453 Genotyping was performed at the Center for Applied Genomics Core at Children's Hospital of
454 Pennsylvania (CHOP). We performed QC on SNP arrays using GenomeStudio v2.0[127,128],
455 retaining patient genotypes with call rate of >95% of SNPs, and SNPs with minor allele frequency
456 (MAF) >0.2, call rate >99%, and clustering ("GenTrain") score >0.7. We performed a second
457 round of SNP genotyping for three donors with SNP call rates <95%, resulting in two panels with
458 517,091 SNPs (614,679 variants total) and 416,166 SNPs (603,685 variants total) across
459 chromosomal designations 1-22, X, Y, XY, PAR, and MT. To create a demultiplexing reference,
460 we retained SNPs from chromosomes 1-22 for each panel, and we imputed larger arrays for these
461 to improve demultiplexing accuracy[30] using the Trans-Omics for Precision Medicine (TOPMed)
462 Imputation Server[129–131] (TOPMed r2 reference, EAGLE v2.4 phasing[132,133], no r^2 filter, data-
463 TOPMed reference panel allele frequency comparisons, pre-run QC). After pre-run QC, 482,995
464 and 212,783 SNPs from the two panels were used for phasing and imputation; after imputation
465 the panels had 27,749,087 and 11,426,093 SNPs. We combined these imputed genotypes for
466 donors into a single reference and ran demuxlet on each group of sequenced libraries we produced
467 as described above (4 total). For each group, we filtered the demultiplexing reference using
468 bcftools[134] to retain only biallelic SNPs that had a depth of coverage across donors >9, as well as
469 estimated imputation accuracy r^2 >0.5 and MAF >0.2. Our resulting reference panels included
470 568,817; 480,835; 676,322; and 291,170 SNPs.
471
472 ***Alignment and cleaning of snRNA-seq data***
473 We pre-processed sequenced data using multiple steps, first performing alignment,
474 demultiplexing, and expression noise/doublet removal on each pooled library separately, then
475 performing heuristic-based filtering on the data from all libraries combined, to generate per-donor
476 data cleaned of ambient RNA, doublets, and other low-quality information.
477
478 *1. Read alignment*
479 We first aligned reads per library to a composite genome using Cellranger version 6.1.2 (using
480 *count* with option *--include-introns*)[135,136]. We built the composite genome reference using
481 CellRanger's *mkref*, to be a combination of the GRCh38 human genome, the mm10 mouse
482 genome, and a split version of the HIV-1 reference genome (previously shown to reduce
483 ambiguities in alignment of HIV-associated reads, increasing detection[137]). Notably, we only
484 detected two HIV reads in our data, likely related to both the presence of highly mutated HIV
485 dissimilar to the reference sequence and lower viral levels in our chronically infected, non-
486 encephalitic HIV+ donors (Discussion).
487
488 *2. Demultiplexing/multidonor doublet removal (demuxlet) + expression noise removal*
489 *(CellBender)*
490 Second, we performed two processes in parallel, demultiplexing and ambient RNA/noise
491 removal, using as input for each the human-genome-aligned reads for each library. We
492 demultiplexed data with demuxlet[30] and popscle (https://github.com/statgen/popscle), using our
493 donor SNP reference panel described above, doublet mixing fraction α ranging from 0 to 0.5, and
494 0.1 doublet prior, which produced for each nuclear barcode a label of "singlet", "doublet", or
495 "ambiguous" and its maximum-likelihood donor ID(s). We confirmed that for each library the
496 donor IDs returned matched those expected.
497

498 We performed ambient RNA/noise removal using CellBender remove-background[138,139] with the
499 *remove-background-v3-alpha* workflow on the Terra.bio platform[140,141]. CellBender uses
500 unsupervised learning to model and remove expression count noise, due to ambient RNA
501 molecules and random barcode swapping. For most libraries we ran CellBender using false
502 positive rate 0.01, learning rate 0.00005, posterior batch size 5, 150 epochs, and 2 retries. For a
503 few libraries, we adjusted these: CellBender failed to converge during learning for library SNr11
504 with our original parameters but achieved reasonable loss indicative of successful learning with
505 learning rate 0.000025 over 200 epochs. Another library (SNr27) showed signs of overfitting that
506 we corrected by using learning rate 0.00005 over 60 epochs. For each library, the output from
507 CellBender was a cleaned expression matrix in anndata[142] format.
508
509 We combined demuxlet and CellBender results by filtering each library's CellBender-cleaned
510 expression data to retain only demuxlet-assigned, nuclear singlet barcodes, then adding the
511 corresponding donor IDs to the expression data as barcode annotations.
512
513 *3. Multi-cell-type doublet removal (Scrublet)*
514 Third, we used Scrublet[143] to remove remaining doublets (barcodes containing reads from
515 multiple cell types from one patient; we expected that demuxlet removed most multi-patient
516 doublets), processing each patient's nuclei within each library separately (134 patient groups
517 across 51 libraries). Scrublet removed 4,372 doublets in total, or a median (IQR) of 33 (8, 37)
518 (1.45% [0.82%, 2.22%]) of doublet barcodes per group. After this step, we presumed that most
519 barcodes corresponded to single nuclei and subsequently called them "nuclei".
520
521 *4. Heuristic filtering*
522 Fourth, we combined expression data across all libraries and performed heuristic filtering to
523 remove potentially low-quality or dying nuclei. We filtered based on fraction of mitochondrial
524 genes/nucleus, number of genes/nucleus, and number of reads (denoted by unique molecular
525 identifiers or "UMIs")/nucleus. For each heuristic, we produced the distribution of values across
526 all dataset nuclei, then identified the thresholds of specific distribution tails and filtered out nuclei
527 with more extreme values. We excluded nuclei with the highest mitochondrial fractions from our
528 dataset, since fractions >5% or 10% are typically thought to indicate potentially dying cells[31]. We
529 removed nuclei in the upper tail of our dataset, amounting to 10% of our nuclei with
530 mitochondrial fractions >1.28% (Fig. S1A). This measure is notably lower than typical thresholds
531 (5% to 10%), such that we may have conservatively over-removed nuclei in this step. We also
532 removed nuclei with excessively high numbers of genes/nucleus (which may indicate e.g.
533 doublets), excluding the upper tail or the ~5% of our nuclei with >4,396 genes/nucleus (Fig.
534 S1B). Importantly, because previous studies have shown that human SN neurons and some
535 immune cells exhibit lower gene counts in snRNA-seq datasets[31,32], we did not filter out nuclei
536 with lower genes/nucleus at this step. Instead, we relied on cell-type-specific filtering performed
537 during differential expression analysis to exclude low-count data (see below). Following a similar
538 rationale, we excluded nuclei in the upper tail of our dataset in terms of number of UMIs/nuclei,
539 amounting to ~5% of our nuclei with >17,153 UMIs (Fig. S1C). Notably, we identified heuristic
540 thresholds each time a new group of sequenced data was added to our dataset (during data
541 generation; see above) and identified roughly the same thresholds as those above during each
542 intermediate stage.
543
544 ***snRNA-seq data dimensionality reduction, batch correction, and nucleus clustering***
545 To produce a finalized dataset for analysis, we performed three additional steps. First, we further
546 reduced expression count noise using two forms of linear dimensionality reduction: highly
547 variable gene (HVG) selection and principal component analysis (PCA) dimensionality reduction

548 (Figs. S1E, F). Second, we performed batch correction, to facilitate cross-library dataset
549 integration (Data S5). Third, we performed nucleus clustering to use as input for cell typing.
550 Below, we explain several choices that we made in these steps to accommodate expected
551 transcriptional abnormalities for donors. Many of these and other downstream analyses were
552 performed using scanpy[144] and other packages as noted.
553
554 When selecting HVGs (scanpy.pp.highly_variable_genes() with "seurat_v3" option, which ranks
555 genes by cross-nucleus variance[33]), we found that the top 2,000 HVGs excluded many marker
556 genes we used for cell typing, and included genes, like inflammatory markers, that might relate
557 more to cell state. To retain more cell type marker genes but still reduce noise, we ordered all
558 36,601 genes in our data by increasing HVG rank (decreasing expression variance) and inspected
559 the simultaneous decrease in minimum expression variance and increase in number of cell type
560 marker genes as we considered more HVGs (Fig. S1E). We selected a number of HVGs to retain
561 that was past the elbow of the "number of cell type marker genes" curve, because beyond this
562 point, including additional HVGs would introduce cell type marker genes at slower rates at the
563 cost of adding progressively lower-variance data (a diminishing return). We kept 20,000 HVGs,
564 which preserved 67% of our database's cell type marker genes (Data S6). Notably, working with
565 this number of HVGs posed a substantial memory burden, since several scanpy functions by
566 default convert expression counts to high-precision data types (64-bit). To alleviate this burden,
567 we created modified versions of several scanpy functions for downstream analysis that
568 maintained data at a user-specified precision; we then found the smallest data precision that
569 would accommodate our expression data (32-bit) and used it as input to those functions.
570
571 We performed PCA on HVG-selected expression data (scanpy.tl.pca()) and retained the first 25
572 components (Fig. S1F) for batch correction and also UMAP (Uniform Manifold Approximation
573 and Projection)[145,146] generation, clustering, and other downstream analysis. We preserved PCA-
574 reduced, batch-corrected expression data for downstream analysis by projecting it back to the
575 barcodes-by-genes basis from the truncated PCA basis (details below). To facilitate this last step,
576 we stored the means and standard deviations used to scale data prior to PCA as well as PCA
577 loadings using a data-type-modified version of scanpy.pp.scale(), with zero centering and no
578 expression count capping (to recover the original counts data in the limit of no PCA truncation or
579 batch correction).
580
581 We ran batch correction using Harmony[147] (snRNA-seq library ID batch variable, 20 maximum
582 iterations); Harmony converged in 3 iterations. We confirmed that batch correction results were
583 reasonable by comparing pre- vs. post- Harmonization 2D UMAP localizations for nuclei that
584 were from the same patient but processed in different libraries (Data S5).
585
586 Batch-corrected data in the PCA basis was used to make a UMAP-based neighborhood
587 connectivity graph using scanpy.pp.neighbors() (20 neighbors) for local manifold approximation;
588 we then generated 2D UMAPs using scanpy.tl.umap() and initial Leiden clusters for cell typing
589 using scanpy.tl.leiden() (resolution parameter 0.5).
590
591 We projected the batch-corrected, scaled expression data back to the gene basis from the PCA
592 basis using the 25 stored PCA loadings, then made the resulting scaled expression data count-like,
593 ensuring non-negative counts, then rescaled it using stored means and standard deviations (Fig.
594 S4). Batch-corrected distributions sometimes had non-negligibly negative values (indicative of
595 barcodes with minimal, effectively zero, HVG counts relative to others). Most of these values
596 were between -1 and 0 (Fig. S4B), and any adjusted count values of <-1 occupied <1% of any
597 given HVG's corrected distribution (Fig. S4C). We thus set these negative values to zero; our

598 approach for doing so was to zero the lowest 1% of each HVG's count distribution. This approach
599 had no effect on existing non-negative count values because a substantial percentage of each
600 HVG's distribution was zero counts. We then shifted each distribution so its minimum matched
601 its uncorrected counterpart and would produce non-negative values upon rescaling. Finally, we
602 rescaled the values, set any remaining negative values to zero, and converted to integer-type.
603
604 ***Likelihood-based cell typing***
605 Because we observed indications of abnormal transcription, we wanted to avoid assumptions
606 about cell types that were present in our data or the most appropriate marker genes to use for cell
607 typing. We thus developed an approach for cell typing based on the principle employed in
608 ScType, a computational cell typing tool[148]. ScType estimates cell types using a large, multi-
609 tissue, multi-organism database of cell-type-specific "positive" and "negative" marker genes that
610 are expressed in or suppressed in a cell type, respectively. For a group of unidentified nuclei or
611 cells and specified tissue(s), ScType computes a "cell type score" for each nucleus and possible
612 cell type, which is a weighted sum of the nucleus's standardized expression levels across the
613 possible cell type's positive and negative marker genes. Weights each reflect a "marker gene
614 specificity score", reducing the impact of less-specific marker genes, and have negative sign for
615 negative marker genes to penalize the score when these are expressed; ScType assigns the cell
616 type with the maximum score to each nucleus.
617
618 Our approach, like ScType's, compares gene expression levels against a cell type marker gene
619 database, but in other respects it differs considerably. We perform cell typing on nuclear clusters
620 rather than individual nuclei, with the reasoning that clusters, by definition, group nuclei with
621 similar transcriptional profiles, and that considering them may highlight genes with characteristic
622 expression levels that may be more helpful for cell typing. We identify such "distinguishing
623 HVGs" for each cluster as the HVGs that are differentially overexpressed vs. all other clusters
624 combined, using scanpy.tl.rank_genes_groups() with *k*-fold, leave-one-out cross-fold validation
625 (k=10) on scaled (scanpy.pp.normalize_total()), log1p-transformed (scanpy.pp.log1p()) data
626 (Wilcoxon-rank-sum comparison, Benjamini-Hochberg p-value correction). We considered genes
627 that were overexpressed across all k=10 calculations with log2 fold change (l2fc) >1.0 and
628 adjusted p <0.01 to be distinguishing HVGs, and we used these (as opposed to all HVGs) for
629 comparison of the nuclear cluster against our cell type marker gene database.
630
631 The cell type database we use in this study is a modified subset of the ScType database[148] that
632 contains marker genes for relevant human tissues (brain, immune tissue, and smooth muscle
633 tissue, which has cell types resembling those in the blood-brain-barrier). Some ScType cell types
634 appeared in multiple tissues, so we removed any redundancies in these, either merging types with
635 identical marker gene lists or assigning tissue-specific names to cell types with differing lists (e.g.
636 renaming "Endothelial Cell" to "Brain Endothelial Cells"). We then added marker genes from
637 recent postmortem human SN snRNA-seq studies[34,149,150] to the database. We also retained cell
638 types not expected for SN (e.g. glutamatergic neurons, fibroblasts, cancer cells) to detect potential
639 sample issues and to better characterize unexpected phenotypes. Finally, although we pulled
640 positive and negative marker genes from ScType and have included an option to use them in our
641 code, we only used positive marker genes in this study, to avoid assuming that negative markers
642 would be absent for cells in non-normative states. The final database that we used in our analysis
643 here has 61 cell types, with median (IQR) 14 (6, 27) positive marker genes per cell type, and 515
644 positive marker genes total (Data S6).
645
646 In our approach, we use likelihoods to assess whether a cluster is of a particular cell type.
647 Explicitly, for a cluster n of nuclei, and cell type c, we define the likelihood L as the joint

probability that each of c's markers, mg_c^i (where i is an identifying index running from 1 to the total number of marker genes M) is a true, defining marker gene for n (meaning that it is in the set of n's distinguishing HVGs, which we denote as mg_n):

$$mg_c^i \in \{mg_n^j\} \tag{1}$$

(where j is another identifying index). We assume that the probability of mg_c^i being a marker for n is a monotonically increasing function of its overexpression level in n, which we denote as $o_{c,i}^n$. By this, we mean that if mg_c^i was not overexpressed in n, its probability of being a marker for n is ~0, and if it is overexpressed, its probability of being a marker increases with increasing $o_{c,i}^n$, saturating at ~1 above some overexpression level:

$$Prob(mg_c^i \in \{mg_n^j\}) \sim f(o_{c,i}^n), f \text{ increasing with } o_{c,i}^n \tag{2}$$

We make an approximation of linear dependence on $o_{c,i}^n$,

$$Prob(mg_c^i \in \{mg_n^j\}) \sim f(o_{c,i}^n) \sim o_{c,i}^n \tag{3}$$

and we make the simplifying assumption that the probability functions for $\{mg_c^i\}$ can reasonably be treated as independent. The likelihood then takes the form

$$L(n,c) = \prod_{i=1}^{M} o_{c,i}^n \tag{4}$$

In our calculations we use the log-likelihood LL:

$$LL(n,c) = \sum_{i=1}^{M} log(o_{c,i}^n) \tag{5}$$

If negative marker genes were to be used (they are not in this study), the log likelihood becomes

$$LL(n,c) = \sum_{i=1}^{Mpos} log(o_{c,i}^n) - \sum_{j=1}^{Mneg} log(o_{c,j}^n) \tag{6}$$

We do not apply cell-type-specificity or other weighting to marker gene likelihood terms, to avoid inadvertently making biased assumptions. For example, by not applying weights, we avoid inappropriately upweighting marker genes that appear for fewer database cell types as a result of missing data rather than biological specificity. We also avoid discounting less-specific marker genes that may nevertheless be informative for cell typing.

We construct the log-likelihood in Eq. (5) by setting $log(o_{c,i}^n)$, the log overexpression for marker gene i of cell type c, to either the mean (across k calculations) l2fc expression of that gene in cluster n if the gene was a distinguishing HVG (and thus significantly overexpressed), or 0 if not (overexpression level $o_{c,i}^n$=1). Using this measure, we observe substantial drop-off in log-likelihood as the overlap between a cluster's distinguishing HVG's and a cell type's marker genes decreases (Fig. S5), leaving only a few putative cell types. We used the highest-likelihood cell types and the contributing database marker genes for each to assign a cell type to each nuclear cluster, and we used this approach in multiple rounds to arrive at final cell types. First, we ran cell typing on our original Leiden clusters, then combined contiguous clusters with the same cell type,

then performed subclustering on any of the resulting clusters that had visible substructure (8 total), again using a Leiden algorithm but with resolution 0.1 on each cluster in isolation. Subclustering had the effect of splitting nuclei groups with different cell types that were originally merged, including microglia and macrophages, and GABAergic and dopaminergic neurons. Finally, we performed cell typing again on these re-clustered nuclei, generating the cell types in Fig. 1. We found our cell types to be in agreement with previously published human SN snRNA-seq data[34] (Fig. S3).

Differential expression analysis (DEA)

We performed Wald-formulation DEAs on each cell type separately with *k*-fold cross-validation (*k*=3 set by power analysis; below), using DESeq2 [43] ported into Python with the package diffexpr (https://github.com/wckdouglas/diffexpr/tree/master). For SUD+ vs. SUD- comparisons, the generalized linear model (GLM) we used as DESeq2 input was

$$\begin{gathered} gene\ expression\ level \sim HIV\ level, SUD_{opc}\ donor\ group\ + SUD_{other} + \\ age\ +\ sex\ +\ race\ +\ ethnicity\ + \\ overdose\ death\ status\ +\ PMI\ +\ tissue\ location\ + \\ CD4\ nadir \end{gathered} \tag{7}$$

For HIV comparisons (HIV+u vs. HIV-; HIV+d vs. HIV-; HIV+d vs. HIV+u), our GLM was

$$\begin{gathered} gene\ expression\ level \sim HIV\ level, SUD_{opc}\ donor\ group +\ SUD_{other} + \\ age\ +\ sex\ +\ race\ +\ ethnicity\ + \\ overdose\ death\ status\ +\ PMI\ +\ tissue\ location \end{gathered} \tag{8}$$

Covariates are defined as follows:

HIV level: Categorical. Final HIV viral load in copies RNA/mL. (Options are "HIV-", "HIV+u" for <50 copies/mL, "HIV+d" for ≥50 copies/mL)

SUD_{opc}: Categorical. Presence of opioid and/or cocaine SUD diagnosis. ("yes", "no")

SUD_{other}: Categorical. Presence of SUD diagnosis for substance other than opioids/cocaine. ("yes", "no")

Age: Numeric. Donor age in years.

Sex: Categorical. Donor sex assigned at birth. ("female", "male")

Race: Categorical. Donor race described in clinical records. ("Black or African American", "White", "Asian", "Black and White", "Black and Indian", "Unknown or Not Reported")

Ethnicity: Categorical. Donor ethnicity described in clinical records. ("Hispanic or Latino", "Not Hispanic or Latino")

Overdose Death Status: Categorical. Presence of overdose as cause of death. ("yes", "no")

Postmortem Interval (PMI): Numeric. Donor post-mortem interval in hours.

Tissue Location: Categorical. Approximate anatomical location of SN sample. ("coronal" for rostral midbrain, "midbrain" for caudal midbrain)

CD4 Nadir: Categorical. Lowest donor CD4 T-cell count. ("<200 cells/μL", "[200,500] cells/μL", ">500 cells/μL"). HIV- donors are assigned ">500 cells/μL".

Prior to running DESeq2, numerical covariates were standardized, and categorical covariates that covaried perfectly were identified, and all but one were removed, to avoid ambiguity in fitting. None of the DEAs in this study required us to drop covariates.

DESeq2 implements multiple controls to remove false positives[43], and we used *k*-fold cross-validation as an additional layer of false positive control for each DEA. In *k*-fold cross-validation,

random subsetting of data is expected to randomly alter low gene dispersions. Low dispersions can exist for genes with prominent within-donor correlations (e.g. if there are many similar nuclei per donor relative to the rest of the DEA data) and/or low counts, and they can inflate the apparent effect size of expression changes, leading to false positives. The randomly altered dispersions across *k*-fold cross-validation computations alters the degree to which such genes are false positives. We filtered to include only DEGs that show up in all *k* random subsets (below), which helps to remove these impacts. DESeq2 can also be run on single-nucleus data rather than pseudobulked data (for which nuclei are aggregated per cell type and donor); the single-nucleus approach can help to highlight DEGs that may be pertinent to subsets of a cell type if the nuclei exhibit biological variability[42], and for this reason we ran DESeq2 on our single-nucleus data without pseudobulking. DESeq2 authors have made recommendations for run parameters that increase the number of "true positive" DEGs returned when running on single-nucleus data by handling zero inflation characteristic of single-cell approaches[42]; we have confirmed that those recommendations reproduce our results and add additional DEGs. Importantly, our procedure is more restrictive in terms of DEGs returned but still benefits from false positive controls and does not produce DEGs not seen when run with DESeq2-author-recommended parameters. One comparison is shown below for DEA results using our parameters (Wald test, useT=False, default sizeFactors, and pseudocount addition) vs. zero-inflation recommendations (likelihood ratio test, useT=True, minmu=1e-6, sizeFactors from scran::computeSumFactors).

Cell type	DEA	N up DEGs reported in our paper	N up DEGs common to both approaches	N down DEGs reported in our paper	N down DEGs common to both approaches
DA	SUD+HIV- vs. SUD-HIV-	0	0	51	49
DA	SUD+HIV+u vs. SUD-HIV+u	82	76	41	41
DA	SUD+HIV+d vs. SUD-HIV+d	0	0	0	0

To perform DEA, we formed *k* data subsets from a cell type's nuclei, then fit the DESeq2 model to each subset (using the GLM in Eq. 7 when assessing SUD impacts or Eq. 8 when assessing HIV impacts; py_DESeq2() followed by run_deseq()). We then pulled the results for each donor group comparison of interest (e.g. SUD+HIV- vs. SUD-HIV- donor groups) using dds.deseq_result(). With this approach, DEA model fitting for each *k*th subset was based on nuclei from ~90 donors across all donor groups, such that fits of gene dispersion benefitted from a large sample size and higher nuclear variability. We identified differentially expressed genes (DEGs) as those with adjusted p-values <0.05 across all *k* calculations. For significant DEGs, we used the cross-fold means of l2fc and normalized counts in Figs. 2-5 and for gene set enrichment analysis.

We included an extra term in our SUD GLM (Eq. 7), for CD4 T cell nadir, that was not in our HIV GLM (Eq. 8). This is because, although we split HIV groups by the clinically relevant measure of final VL, we noted that other lifetime characteristics of HIV infection could impact transcription, most notably long-term damage incurred during periods of low T-cell counts. We thus added CD4 nadir to Eq. 7 to account for longer-term HIV impacts, and to aid detection of SUD impacts. We found that CD4 nadir tracked closely with final HIV VL for our HIV+ donors, accounting for a small degree of HIV-related variation. For HIV comparisons, we excluded CD4 nadir because it closely recapitulated HIV VL variation.

787 ***Gene set enrichment analysis (GSEA)***
788 We performed GSEA with Enrichr[44] using GSEApy, a Python wrapper for R-based GSEA
789 tools[151]. For each DEA, we ran Enrichr separately for up- and down- regulated DEGs
790 (gseapy.enrichr()), using our 20,000 HVGs as background and human annotated gene set
791 reference "GO_Biological_Process_2023"[152,153]. We saved all gene sets returned regardless of
792 significance but considered gene sets with adjusted p-value <0.05 to be significantly endorsed
793 (Data S2). We also tested the tool GSEA[154,155] in GSEApy, and found that it identified similar but
794 generally fewer significant gene sets for DEGs (Table S7, Data S9).
795
796 ***Identification of highly coordinated DEG subclusters***
797 To find DEG subclusters for a particular DEA and set of cell types, we first pulled the normalized
798 count data (scanpy.pp.normalize_total(); as opposed to l2fc or any other DEA result), for all
799 nuclei of each cell type of interest, across all that DEA's case group donors. We then computed
800 for each cell type, each DEG's mean normalized expression count (across all that cell type's
801 nuclei) per case donor. This step produced a matrix of cell-type-specific DEGs per row, and the
802 mean normalized expression of that DEG for each case donor per column. To distinguish DEGs
803 that arose for multiple cell types, and to keep track of the direction of dysregulation, we named
804 DEGs using the convention c*ell-type_DEG-direction_gene-name*. For all DEGs across all cell
805 types, we then computed cross-donor Pearson correlations in mean expression for DEG pairs
806 using scipy.stats.pearsonr(), using the built-in beta-assumption hypothesis test to determine
807 significance (two-tailed alternative) with significance level 0.05. Across all our computations
808 (Table S8) there were median (IQR) 30% (28%, 34%) DEG pairs with significant correlations.
809
810 We computed the similarity for each DEG pair to be the correlation magnitude if it was
811 significant or 0 if not significant; for DEGs *i,j*
812
813 $$similarity_{i,j} = sim_{i,j} = abs(r_{i,j}), p_{i,j} < 0.05;\ 0\ otherwise \quad (9)$$
814
815 To use hierarchical agglomerative clustering to group DEGs, we transformed similarities to
816 distances using
817
818 $$dist_{i,j} = \frac{1}{(1 + sim_{i,j})} \quad (10)$$
819
820 adding 1 to the similarity to avoid division by zero. We used Eq. 10 instead of $dist_{i,j} = 1 -$
821 $sim_{i,j}$ because its nonlinearity required DEG clusters to have more pronounced similarity to be
822 detected, by inflating distances between higher-similarity DEG pairs, and thus by suppressing the
823 dynamic range of distances used to parse clusters. We performed clustering using
824 sklearn.cluster.AgglomerativeClustering() (average linkage distance) with "distance_threshold"=0
825 and "n_clusters"=None to compute the entire linkage tree and return algorithm-generated DEG
826 clusters. The resulting DEG clusters often contained noticeable subclusters, with inter-subcluster
827 distances substantially larger than intra-group distances. We thus split them at points where the
828 distance between adjacent DEGs was ≥3 standard deviations above the cluster's mean adjacent
829 DEG distance. To keep track of original cluster identity, we named DEG subclusters using the
830 convention C*[cluster-index]*S*[subcluster-index]* (e.g. "C17S2" for cluster 17, subcluster 2). We
831 characterized subcluster coordination strength by computing the average similarity across all
832 DEG pairs in a subcluster. Some subclusters had exceptionally low average similarities (~0.2 vs.
833 ~0.8; Fig. 6A, right), indicating weaker overall relationships with other DEGs. To focus on
834 annotating the most highly coordinated DEG groups, we removed these low-similarity clusters by

excluding anything in the lower tail of the distribution of average similarities across all DEG subclusters (<0.75; Fig. 6A right).

DEG subcluster annotations

We produced a skeleton annotation .csv file for each DEG subcluster using "GO_Biological_Process_2023" annotations and the acyclic graph of their relationships ("go-basic.obo"). For each DEG, we found all related GO terms and filtered them to include only the most subordinate annotation represented on each graph branch (most specific process). We split remaining terms into those explicitly mentioning positive regulation of a process, explicit negative regulation, explicit response, and others, as an initial basis for annotation (Data S3). We used DEG naming convention *cell-type_DEG-direction_gene-name* to facilitate interpretation.

For focused DEG subcluster annotations, two experts (MJ, AW) independently searched different gene databases for each DEG (MJ, GeneCards; AW, National Center for Biotechnology Information gene database) and pulled the functional summary. They then performed a literature search for the DEG using terms related to HIV, SUD, brain location ("substantia nigra", "ventral midbrain"), and cell type (e.g. "gene *x* in neurons", "gene *x* in dopaminergic neurons", "gene *x* in microglia"). Relevant references were collected and used to annotate potentially relevant functions for each gene; these results were then used to generate a consensus across annotators that was used in each DEG subcluster (Data S4).

Statistical analysis

snRNA-seq sample size selection

We used a power analysis simulation to estimate the number of nuclei per donor needed to power detection of cell-type-specific expression differences. We simulated a case where expression data was compared across two groups for one gene in one cell type, and there was a small but true difference in the two distributions. We defined each group's underlying expression distribution for the gene to have a lognormal distribution, i.e.

$$Prob(x\ counts) \sim Lognormal(\mu, \sigma^2) \ = \ exp(N(\mu, \sigma^2)) \tag{11}$$

We let both distributions have the same variance of 1 and means differing by some l2fc value. The difference between means μ_1 and μ_2 was related to the l2fc by

$$abs(\mu_1 - \mu_2) = log_e(2^{log2fc}) \tag{12}$$

For each l2fc we tested (0.5, 1.0, 1.5), we defined the two underlying distribution means using Eq. 12, then over 10,000 iterations sampled distributions of size *s* (nuclei) from each and performed a Wilcoxon rank sum test of distinguishability. We computed the power as the fraction of iterations in which the true difference was detected ($p < 0.05$). We repeated this simulation starting with s=10 and incrementing s by 2 until we reached a power ≥80%. We achieved sufficient detection power with s=158 for l2fc 0.5; s=42 for l2fc 1.0; and s=20 for l2fc 1.5. Based on this simplified situation, we set a threshold of ~100 nuclei per cell type, aiming for detection of expression differences at l2fc 1.0. Prior to analysis, we estimated there would be ~10 expected cell types in SN (DA and GABA neurons, microglia, astrocytes, ODCs, OPCs, multiple blood-brain-barrier cells, multiple immune cells[149,156]) and thus aimed to sequence 1,000 nuclei per donor.

Overexpression level and k selection for cluster "distinguishing HVG" detection

We used a similar power analysis to estimate the l2fc at which distinguishing HVG detection was powered for every cluster of nuclei. We set a significance threshold of p=0.01 to restrict detected distinguishing HVGs to a higher-confidence subset, since these could impact cell typing and thus all downstream analysis. We let distributions represent expression of a gene for one cluster vs. the rest, choosing normal distributions with equal variance and differing means to reflect log1p pre-processing (applied for scanpy.tl.rank_genes_groups()). The means and l2fc were related by

$$\mu_1 = 1, \mu_2 = 2^{log2fc} \tag{13}$$

At l2fc=1.0, every cluster exceeded the minimum sample size for 80% detection power. We determined the number of folds *k* for cross-validation by increasing *k* from 2 in increments of 1 until every cluster with one of its *k* folds removed had enough nuclei to also power detection. Our code also had an option for the resulting *k* to be increased by 1, to put each one-fold-removed group of nuclei further over the power detection threshold during cross-fold validation calculations. We enabled this option, finding *k*=9 and using *k*=10.

Overexpression threshold and k selection for DEA

We used the same power simulation to estimate the values of l2fc and *k* that would power DEAs for each cell type at p=0.05, using *k*=3 and l2fc=1.0.

Significance testing of cell type proportions across donor groups

We tested cell type proportions were differently represented across donor groups by first using the binomial distribution to model cell type proportions for each donor group. For a donor with *k* nuclei of a specified cell type and *n* nuclei total, the maximum likelihood estimation for the probability of that cell type's occurrence, $\hat{p}$, is

$$\hat{p} = \frac{k}{n} \tag{14}$$

Within each donor group, we computed for each donor the $\hat{p}$ for each cell type, producing a distribution of each cell type's occurrence probability across group donors. For each cell type, we performed Kolmogorov-Smirnov tests to compare these distributions for each pair of donor groups, using Benjamini-Hochberg multiple comparison correction (12 comparisons, one per cell type, per donor group pair). We considered donor group pairs/cell types with adjusted p <0.05 to have significant differences (Table S5).

Significance test for DEG overlaps

We performed random sampling tests to determine whether fractions of overlapping DEGs observed for related DEAs (Figs. 2-5) were significantly different from expected outcomes of random sampling. For each DEA pair, we sampled the observed numbers of DEGs per DEA from the 20,000-HVG background, and we recorded the fraction of overlapping DEGs between the two simulated populations. We repeated sampling for 100,000 iterations and computed the upper limit on the p-value to be the fraction of iterations with at least as many overlapping DEGs as observed. In all tests we found 0 such iterations, corresponding to $p<10^{-5}$.

929 **References**

930 1. The path that ends AIDS: UNAIDS Global AIDS Update 2023.
931 https://www.unaids.org/en/resources/documents/2023/global-aids-update-2023.
932 2. Full report — In Danger: UNAIDS Global AIDS Update 2022.
933 https://www.unaids.org/en/resources/documents/2022/in-danger-global-aids-update.
934 3. Le, L. T. & Spudich, S. S. HIV-Associated Neurologic Disorders and Central Nervous
935 System Opportunistic Infections in HIV. *Semin. Neurol.* **36**, 373–381 (2016).
936 4. Clifford, D. B. & Ances, B. M. HIV-associated neurocognitive disorder. *Lancet Infect. Dis.*
937 **13**, 976–986 (2013).
938 5. Wang, S.-C. & Maher, B. Substance use disorder, intravenous injection, and HIV infection:
939 A review. *Cell Transplant.* **28**, 1465–1471 (2019).
940 6. Klevens, R. M., Hu, D. J., Jiles, R. & Holmberg, S. D. Evolving epidemiology of hepatitis C
941 virus in the United States. *Clin. Infect. Dis.* **55 Suppl 1**, S3-9 (2012).
942 7. Moss, R. & Munt, B. Injection drug use and right sided endocarditis. *Heart* **89**, 577–581
943 (2003).
944 8. Kelly, T. M. & Daley, D. C. Integrated treatment of substance use and psychiatric disorders.
945 *Soc. Work Public Health* **28**, 388–406 (2013).
946 9. Gupta, A. *et al.* Evaluation of Hepatitis C Treatment Outcomes Among Patients Enrolled in
947 Outpatient Parenteral Antibiotic Therapy-Boston, Massachusetts, 2016-2021. *Open Forum*
948 *Infect Dis* **10**, ofad342 (2023).
949 10. Volkow, N. D. & Blanco, C. Substance use disorders: a comprehensive update of
950 classification, epidemiology, neurobiology, clinical aspects, treatment and prevention. *World*
951 *Psychiatry* **22**, 203–229 (2023).
952 11. Zhang, Y. *et al.* The Impact of Substance Use on Adherence to Antiretroviral Therapy
953 Among HIV-Infected Women in the United States. *AIDS Behav.* **22**, 896–908 (2018).

954 12. Hinkin, C. H. *et al.* Drug use and medication adherence among HIV-1 infected individuals.
955 *AIDS Behav.* **11**, 185–194 (2007).
956 13. Cohn, S. E. *et al.* Association of ongoing drug and alcohol use with non-adherence to
957 antiretroviral therapy and higher risk of AIDS and death: results from ACTG 362. *AIDS Care*
958 **23**, 775–785 (2011).
959 14. Bangsberg, D. R., Ragland, K., Monk, A. & Deeks, S. G. A single tablet regimen is
960 associated with higher adherence and viral suppression than multiple tablet regimens in
961 HIV+ homeless and marginally housed people. *AIDS* **24**, 2835–2840 (2010).
962 15. de Wit, H. Impulsivity as a determinant and consequence of drug use: a review of underlying
963 processes. *Addict. Biol.* **14**, 22–31 (2009).
964 16. Purohit, V., Rapaka, R. & Shurtleff, D. Drugs of abuse, dopamine, and HIV-associated
965 neurocognitive disorders/HIV-associated dementia. *Mol. Neurobiol.* **44**, 102–110 (2011).
966 17. Ilango, A. *et al.* Similar roles of substantia nigra and ventral tegmental dopamine neurons in
967 reward and aversion. *J. Neurosci.* **34**, 817–822 (2014).
968 18. Wise, R. A. Roles for nigrostriatal--not just mesocorticolimbic--dopamine in reward and
969 addiction. *Trends Neurosci.* **32**, 517–524 (2009).
970 19. Koob, G. F. & Volkow, N. D. Neurocircuitry of addiction. *Neuropsychopharmacology* **35**,
971 217–238 (2010).
972 20. Berridge, K. C. The debate over dopamine's role in reward: the case for incentive salience.
973 *Psychopharmacology (Berl.)* **191**, 391–431 (2007).
974 21. Namba, M. D., Xie, Q. & Barker, J. M. Advancing the preclinical study of comorbid
975 neuroHIV and substance use disorders: Current perspectives and future directions. *Brain*
976 *Behav. Immun.* **113**, 453–475 (2023).

977 22. Nickoloff-Bybel, E. A. *et al.* Dopamine increases HIV entry into macrophages by increasing
978 calcium release via an alternative signaling pathway. *Brain Behav. Immun.* **82**, 239–252
979 (2019).
980 23. Gaskill, P. J. *et al.* Human immunodeficiency virus (HIV) infection of human macrophages is
981 increased by dopamine: a bridge between HIV-associated neurologic disorders and drug
982 abuse. *Am. J. Pathol.* **175**, 1148–1159 (2009).
983 24. Obermann, M. *et al.* Substantia nigra hyperechogenicity and CSF dopamine depletion in
984 HIV. *J. Neurol.* **256**, 948–953 (2009).
985 25. Purohit, V. *et al.* National Institute on Drug Abuse symposium report: drugs of abuse,
986 dopamine, and HIV-associated neurocognitive disorders/HIV-associated dementia. *J.*
987 *Neurovirol.* **19**, 119–122 (2013).
988 26. Kumar, A. M. *et al.* Human immunodeficiency virus type 1 in the central nervous system
989 leads to decreased dopamine in different regions of postmortem human brains. *J. Neurovirol.*
990 **15**, 257–274 (2009).
991 27. Battjes, R. J., Pickens, R. W., Haverkos, H. W. & Sloboda, Z. HIV risk factors among
992 injecting drug users in five US cities. *AIDS* **8**, 681–687 (1994).
993 28. Bertholet, N., Winter, M. R., Heeren, T., Walley, A. Y. & Saitz, R. Polysubstance Use
994 Patterns Associated With HIV Disease Severity Among Those With Substance Use
995 Disorders: A Latent Class Analysis. *J. Stud. Alcohol Drugs* **84**, 79–88 (2023).
996 29. Karamouzian, M., Pilarinos, A., Hayashi, K., Buxton, J. A. & Kerr, T. Latent patterns of
997 polysubstance use among people who use opioids: A systematic review. *Int. J. Drug Policy*
998 **102**, 103584 (2022).
999 30. Kang, H. M. *et al.* Multiplexed droplet single-cell RNA-sequencing using natural genetic
1000 variation. *Nat. Biotechnol.* **36**, 89–94 (2018).

1001 31. Subramanian, A., Alperovich, M., Yang, Y. & Li, B. Biology-inspired data-driven quality
1002 control for scientific discovery in single-cell transcriptomics. *Genome Biol.* **23**, 267 (2022).
1003 32. Welch, J. D. *et al.* Single-cell multi-omic integration compares and contrasts features of brain
1004 cell identity. *Cell* **177**, 1873-1887.e17 (2019).
1005 33. Stuart, T. *et al.* Comprehensive Integration of Single-Cell Data. *Cell* **177**, 1888-1902.e21
1006 (2019).
1007 34. Wei, J. *et al.* Single nucleus transcriptomics of ventral midbrain identifies glial activation
1008 associated with chronic opioid use disorder. *Nat. Commun.* **14**, 5610 (2023).
1009 35. Kamath, T. *et al.* Single-cell genomic profiling of human dopamine neurons identifies a
1010 population that selectively degenerates in Parkinson's disease. *Nat. Neurosci.* **25**, 588–595
1011 (2022).
1012 36. Ostrowski, N. L. & Pert, A. Substantia nigra opiate receptors on basal ganglia efferents.
1013 *Brain Res. Bull.* **38**, 513–523 (1995).
1014 37. Ting-A-Kee, R. & van der Kooy, D. The neurobiology of opiate motivation. *Cold Spring*
1015 *Harb. Perspect. Med.* **2**, (2012).
1016 38. Galaj, E. *et al.* Dissecting the Role of GABA Neurons in the VTA versus SNr in Opioid
1017 Reward. *J. Neurosci.* **40**, 8853–8869 (2020).
1018 39. Nickoloff-Bybel, E. A., Calderon, T. M., Gaskill, P. J. & Berman, J. W. HIV
1019 Neuropathogenesis in the Presence of a Disrupted Dopamine System. *J. Neuroimmune*
1020 *Pharmacol.* **15**, 729–742 (2020).
1021 40. Plaza-Jennings, A. & Akbarian, S. Genomic Exploration of the Brain in People Infected with
1022 HIV-Recent Progress and the Road Ahead. *Curr. HIV/AIDS Rep.* **20**, 357–367 (2023).
1023 41. Thomas, D. M., Francescutti-Verbeem, D. M. & Kuhn, D. M. Gene expression profile of
1024 activated microglia under conditions associated with dopamine neuronal damage. *FASEB J.*
1025 **20**, 515–517 (2006).

1026 42. Van den Berge, K. *et al.* Observation weights unlock bulk RNA-seq tools for zero inflation
1027 and single-cell applications. *Genome Biol.* **19**, 24 (2018).
1028 43. Love, M. I., Huber, W. & Anders, S. Moderated estimation of fold change and dispersion for
1029 RNA-seq data with DESeq2. *Genome Biol.* **15**, 550 (2014).
1030 44. Chen, E. Y. *et al.* Enrichr: interactive and collaborative HTML5 gene list enrichment analysis
1031 tool. *BMC Bioinformatics* **14**, 128 (2013).
1032 45. Gu, L., Caprioli, J. & Piri, N. Rbfox1 expression in amacrine cells is restricted to GABAergic
1033 and VGlut3 glycinergic cells. *Biosci. Rep.* **42**, (2022).
1034 46. Vuong, C. K. *et al.* Rbfox1 Regulates Synaptic Transmission through the Inhibitory Neuron-
1035 Specific vSNARE Vamp1. *Neuron* **98**, 127-141.e7 (2018).
1036 47. Law, P. Y., Hom, D. S. & Loh, H. H. Opiate receptor down-regulation and desensitization in
1037 neuroblastoma X glioma NG108-15 hybrid cells are two separate cellular adaptation
1038 processes. *Mol. Pharmacol.* **24**, 413–424 (1983).
1039 48. Lane, C. M., Elde, R., Loh, H. H. & Lee, N. M. Regulation of an opioid-binding protein in
1040 NG108-15 cells parallels regulation of delta-opioid receptors. *Proc. Natl. Acad. Sci. U. S. A.*
1041 **89**, 11234–11238 (1992).
1042 49. Zhang, Z. *et al.* The Schizophrenia Susceptibility Gene OPCML Regulates Spine Maturation
1043 and Cognitive Behaviors through Eph-Cofilin Signaling. *Cell Rep.* **29**, 49-61.e7 (2019).
1044 50. Darling, T. K. & Lamb, T. J. Emerging Roles for Eph Receptors and Ephrin Ligands in
1045 Immunity. *Front. Immunol.* **10**, 1473 (2019).
1046 51. McClelland, A. C., Sheffler-Collins, S. I., Kayser, M. S. & Dalva, M. B. Ephrin-B1 and
1047 ephrin-B2 mediate EphB-dependent presynaptic development via syntenin-1. *Proc. Natl.*
1048 *Acad. Sci. U. S. A.* **106**, 20487–20492 (2009).
1049 52. Radhakrishna, U. *et al.* Maternal opioid use disorder: Placental transcriptome analysis for
1050 neonatal opioid withdrawal syndrome. *Genomics* **113**, 3610–3617 (2021).

1051 53. Seney, M. L. *et al.* Transcriptional alterations in dorsolateral prefrontal cortex and nucleus
1052 accumbens implicate neuroinflammation and synaptic remodeling in opioid use disorder.
1053 *Biol. Psychiatry* **90**, 550–562 (2021).
1054 54. Phan, B. N. *et al.* Single nuclei transcriptomics in human and non-human primate striatum in
1055 opioid use disorder. *Nat. Commun.* **15**, 878 (2024).
1056 55. Walss-Bass, C. Features of opioid use disorder: Interlinking transcriptomics, epigenetics, and
1057 postmortem studies highlight opioid-induced neurovascular alterations. in *Handbook of the*
1058 *Biology and Pathology of Mental Disorders* 1–15 (Springer International Publishing, Cham,
1059 2024).
1060 56. Byrd, D., Murray, J., Safdieh, G. & Morgello, S. Impact of opiate addiction on
1061 neuroinflammation in HIV. *J. Neurovirol.* **18**, 364–373 (2012).
1062 57. Sumbria, D., Berber, E., Mathayan, M. & Rouse, B. T. Virus Infections and Host
1063 Metabolism-Can We Manage the Interactions? *Front. Immunol.* **11**, 594963 (2020).
1064 58. Maginnis, M. S. β-arrestins and G protein-coupled receptor kinases in viral entry: A
1065 graphical review. *Cell. Signal.* **102**, 110558 (2023).
1066 59. Bieberich, E. Synthesis, Processing, and Function of N-glycans in N-glycoproteins. *Adv*
1067 *Neurobiol* **9**, 47–70 (2014).
1068 60. Lu, X. *et al.* Deficiency of α1,6-fucosyltransferase promotes neuroinflammation by
1069 increasing the sensitivity of glial cells to inflammatory mediators. *Biochim. Biophys. Acta*
1070 *Gen. Subj.* **1863**, 598–608 (2019).
1071 61. Bradberry, M. M., Peters-Clarke, T. M., Shishkova, E., Chapman, E. R. & Coon, J. J. N-
1072 glycoproteomics of brain synapses and synaptic vesicles. *Cell Rep.* **42**, 112368 (2023).
1073 62. Gu, W. *et al.* α1,6-Fucosylation regulates neurite formation via the activin/phospho-Smad2
1074 pathway in PC12 cells: the implicated dual effects of Fut8 for TGF-β/activin-mediated
1075 signaling. *FASEB J.* **27**, 3947–3958 (2013).

1076 63. Fukuda, T. *et al.* Alpha1,6-fucosyltransferase-deficient mice exhibit multiple behavioral
1077 abnormalities associated with a schizophrenia-like phenotype: importance of the balance
1078 between the dopamine and serotonin systems. *J. Biol. Chem.* **286**, 18434–18443 (2011).
1079 64. Guan, S., Zhao, L. & Peng, R. Mitochondrial Respiratory Chain Supercomplexes: From
1080 Structure to Function. *Int. J. Mol. Sci.* **23**, (2022).
1081 65. Xia, D. *et al.* Structural analysis of cytochrome bc1 complexes: implications to the
1082 mechanism of function. *Biochim. Biophys. Acta* **1827**, 1278–1294 (2013).
1083 66. Connor, S. A. *et al.* Altered Cortical Dynamics and Cognitive Function upon
1084 Haploinsufficiency of the Autism-Linked Excitatory Synaptic Suppressor MDGA2. *Neuron*
1085 **91**, 1052–1068 (2016).
1086 67. Toledo, A. *et al.* MDGAs are fast-diffusing molecules that delay excitatory synapse
1087 development by altering neuroligin behavior. *Elife* **11**, (2022).
1088 68. Himes, B. E. *et al.* Genome-wide association analysis in asthma subjects identifies SPATS2L
1089 as a novel bronchodilator response gene. *PLoS Genet.* **8**, e1002824 (2012).
1090 69. Broad, K. D. *et al.* Isoflurane Exposure Induces Cell Death, Microglial Activation and
1091 Modifies the Expression of Genes Supporting Neurodevelopment and Cognitive Function in
1092 the Male Newborn Piglet Brain. *PLoS One* **11**, e0166784 (2016).
1093 70. Duette, G. *et al.* Induction of HIF-1α by HIV-1 Infection in CD4+ T Cells Promotes Viral
1094 Replication and Drives Extracellular Vesicle-Mediated Inflammation. *MBio* **9**, (2018).
1095 71. Deshmane, S. L., Amini, S., Sen, S., Khalili, K. & Sawaya, B. E. Regulation of the HIV-1
1096 promoter by HIF-1α and Vpr proteins. *Virol. J.* **8**, 477 (2011).
1097 72. Xie, W. *et al.* A novel hypoxia-stimulated lncRNA HIF1A-AS3 binds with YBX1 to promote
1098 ovarian cancer tumorigenesis by suppressing p21 and AJAP1 transcription. *Mol. Carcinog.*
1099 **62**, 1860–1876 (2023).

1100 73. Gedam, M. *et al.* Complement C3aR depletion reverses HIF-1α-induced metabolic
1101 impairment and enhances microglial response to Aβ pathology. *J. Clin. Invest.* **133**, (2023).
1102 74. Day, C. J. *et al.* Complement Receptor 3 Mediates HIV-1 Transcytosis across an Intact
1103 Cervical Epithelial Cell Barrier: New Insight into HIV Transmission in Women. *MBio* **13**,
1104 e0217721 (2022).
1105 75. Nomura, N. *et al.* HIV-EP2, a new member of the gene family encoding the human
1106 immunodeficiency virus type 1 enhancer-binding protein. Comparison with HIV-EP1/PRDII-
1107 BF1/MBP-1. *J. Biol. Chem.* **266**, 8590–8594 (1991).
1108 76. Henderson, A. J. & Calame, K. L. CCAAT/enhancer binding protein (C/EBP) sites are
1109 required for HIV-1 replication in primary macrophages but not CD4(+) T cells. *Proc. Natl.*
1110 *Acad. Sci. U. S. A.* **94**, 8714–8719 (1997).
1111 77. Engler, J. R. *et al.* Increased microglia/macrophage gene expression in a subset of adult and
1112 pediatric astrocytomas. *PLoS One* **7**, e43339 (2012).
1113 78. Roman, K. M., Jenkins, A. K., Lewis, D. A. & Volk, D. W. Involvement of the nuclear
1114 factor-κB transcriptional complex in prefrontal cortex immune activation in bipolar disorder.
1115 *Transl. Psychiatry* **11**, 40 (2021).
1116 79. Kuroda, T. S., Fukuda, M., Ariga, H. & Mikoshiba, K. The Slp homology domain of
1117 synaptotagmin-like proteins 1-4 and Slac2 functions as a novel Rab27A binding domain. *J.*
1118 *Biol. Chem.* **277**, 9212–9218 (2002).
1119 80. Gerber, P. P. *et al.* Rab27a controls HIV-1 assembly by regulating plasma membrane levels
1120 of phosphatidylinositol 4,5-bisphosphate. *J. Cell Biol.* **209**, 435–452 (2015).
1121 81. Wang, Z. *et al.* Pro-survival and anti-inflammatory roles of NF-κB c-Rel in the Parkinson's
1122 disease models. *Redox Biol* **30**, 101427 (2020).
1123 82. Rahman, S. M. T. *et al.* Double knockin mice show NF-κB trajectories in immune signaling
1124 and aging. *Cell Rep.* **41**, 111682 (2022).

1125 83. Romani, B., Glashoff, R. H. & Engelbrecht, S. Functional integrity of naturally occurring
1126 mutants of HIV-1 subtype C Vpr. *Virus Res.* **153**, 288–298 (2010).
1127 84. Khan, S. Z., Gasperino, S. & Zeichner, S. L. Nuclear Transit and HIV LTR Binding of NF-
1128 κB Subunits Held by IκB Proteins: Implications for HIV-1 Activation. *Viruses* **11**, (2019).
1129 85. Qi, S. *et al.* Structural basis for ELL2 and AFF4 activation of HIV-1 proviral transcription.
1130 *Nat. Commun.* **8**, 14076 (2017).
1131 86. Yu, D., Liu, R., Yang, G. & Zhou, Q. The PARP1-Siah1 Axis Controls HIV-1 Transcription
1132 and Expression of Siah1 Substrates. *Cell Rep.* **23**, 3741–3749 (2018).
1133 87. Ohno, H. *et al.* Interaction of endocytic signals from the HIV-1 envelope glycoprotein
1134 complex with members of the adaptor medium chain family. *Virology* **238**, 305–315 (1997).
1135 88. Li, M.-T. *et al.* Negative regulation of RIG-I-mediated innate antiviral signaling by
1136 SEC14L1. *J. Virol.* **87**, 10037–10046 (2013).
1137 89. Marschang, P., Sodroski, J., Würzner, R. & Dierich, M. P. Decay-accelerating factor (CD55)
1138 protects human immunodeficiency virus type 1 from inactivation by human complement.
1139 *Eur. J. Immunol.* **25**, 285–290 (1995).
1140 90. Tang, Z. *et al.* CD55 is upregulated by cAMP/PKA/AKT and modulates human
1141 decidualization via Src and ERK pathway and decidualization-related genes. *Mol. Reprod.*
1142 *Dev.* **89**, 256–268 (2022).
1143 91. Lee, C., Wooldridge, T. R. & Laimins, L. A. Analysis of the roles of E6 binding to E6TP1
1144 and nuclear localization in the human papillomavirus type 31 life cycle. *Virology* **358**, 201–
1145 210 (2007).
1146 92. Nishitsuji, H., Sugiyama, R., Abe, M. & Takaku, H. ATP1B3 Protein Modulates the
1147 Restriction of HIV-1 Production and Nuclear Factor κ Light Chain Enhancer of Activated B
1148 Cells (NF-κB) Activation by BST-2. *J. Biol. Chem.* **291**, 4754–4762 (2016).

1149 93. Meeker, R. B., Boles, J. C., Robertson, K. R. & Hall, C. D. Cerebrospinal fluid from human
1150 immunodeficiency virus--infected individuals facilitates neurotoxicity by suppressing
1151 intracellular calcium recovery. *J. Neurovirol.* **11**, 144–156 (2005).
1152 94. Li, Q. S. & De Muynck, L. Differentially expressed genes in Alzheimer's disease
1153 highlighting the roles of microglia genes including OLR1 and astrocyte gene CDK2AP1.
1154 *Brain Behav Immun Health* **13**, 100227 (2021).
1155 95. Aoki, Y. *et al.* LOX-1 mediates inflammatory activation of microglial cells through the p38-
1156 MAPK/NF-κB pathways under hypoxic-ischemic conditions. *Cell Commun. Signal.* **21**, 126
1157 (2023).
1158 96. Borucki, D. M. *et al.* Complement-Mediated Microglial Phagocytosis and Pathological
1159 Changes in the Development and Degeneration of the Visual System. *Front. Immunol.* **11**,
1160 566892 (2020).
1161 97. Marzinke, M. A. & Clagett-Dame, M. The all-trans retinoic acid (atRA)-regulated gene
1162 Calmin (Clmn) regulates cell cycle exit and neurite outgrowth in murine neuroblastoma
1163 (Neuro2a) cells. *Exp. Cell Res.* **318**, 85–93 (2012).
1164 98. Takaishi, M., Ishisaki, Z., Yoshida, T., Takata, Y. & Huh, N.-H. Expression of calmin, a
1165 novel developmentally regulated brain protein with calponin-homology domains. *Brain Res.*
1166 *Mol. Brain Res.* **112**, 146–152 (2003).
1167 99. Salmani, B. Y. *et al.* Transcriptomic atlas of midbrain dopamine neurons uncovers
1168 differential vulnerability in a Parkinsonism lesion model. (2023) doi:10.7554/elife.89482.1.
1169 100. Kari, A. *et al.* Knockdown of EPSTI1 alleviates lipopolysaccharide-induced inflammatory
1170 injury through regulation of NF-κB signaling in a cellular pneumonia model. *Allergol.*
1171 *Immunopathol.* **50**, 106–112 (2022).
1172 101. Wang, Y. *et al.* Identification of IFI44L as a new candidate molecular marker for systemic
1173 lupus erythematosus. *Clin. Exp. Rheumatol.* **41**, 48–59 (2023).

1174 102. Li, Y. *et al.* IFI44L expression is regulated by IRF-1 and HIV-1. *FEBS Open Bio* **11**, 105–
1175 113 (2021).
1176 103. Mertens, J. *et al.* Directly Reprogrammed Human Neurons Retain Aging-Associated
1177 Transcriptomic Signatures and Reveal Age-Related Nucleocytoplasmic Defects. *Cell Stem*
1178 *Cell* **17**, 705–718 (2015).
1179 104. Seibert, M. J., Evans, C. S., Stanley, K. S., Wu, Z. & Chapman, E. R. Synaptotagmin 9
1180 Modulates Spontaneous Neurotransmitter Release in Striatal Neurons by Regulating
1181 Substance P Secretion. *J. Neurosci.* **43**, 1475–1491 (2023).
1182 105. Kozlova, A. A. *et al.* Knock-out of the critical nitric oxide synthase regulator DDAH1 in
1183 mice impacts amphetamine sensitivity and dopamine metabolism. *J. Neural Transm.*
1184 *(Vienna)* **130**, 1097–1112 (2023).
1185 106. Chung, K. M., Jeong, E.-J., Park, H., An, H.-K. & Yu, S.-W. Mediation of Autophagic Cell
1186 Death by Type 3 Ryanodine Receptor (RyR3) in Adult Hippocampal Neural Stem Cells.
1187 *Front. Cell. Neurosci.* **10**, 116 (2016).
1188 107. Balschun, D. *et al.* Deletion of the ryanodine receptor type 3 (RyR3) impairs forms of
1189 synaptic plasticity and spatial learning. *EMBO J.* **18**, 5264–5273 (1999).
1190 108. Murray, J. *et al.* Frontal lobe microglia, neurodegenerative protein accumulation, and
1191 cognitive function in people with HIV. *Acta Neuropathol Commun* **10**, 69 (2022).
1192 109. Bailey, A. J. & McHugh, R. K. Why do we focus on the exception and not the rule?
1193 Examining the prevalence of mono- versus polysubstance use in the general population.
1194 *Addiction* **118**, 2026–2029 (2023).
1195 110. Compton, W. M., Valentino, R. J. & DuPont, R. L. Polysubstance use in the U.S. opioid
1196 crisis. *Mol. Psychiatry* **26**, 41–50 (2021).
1197 111. Rounsaville, B. J., Petry, N. M. & Carroll, K. M. Single versus multiple drug focus in
1198 substance abuse clinical trials research. *Drug Alcohol Depend.* **70**, 117–125 (2003).

1199 112. Fox, H. S. *et al.* Morphine suppresses peripheral responses and transforms brain myeloid
1200 gene expression to favor neuropathogenesis in SIV infection. *Front. Immunol.* **13**, 1012884
1201 (2022).
1202 113. Acharya, A. *et al.* Chronic morphine administration differentially modulates viral reservoirs
1203 in a simian immunodeficiency virus SIVmac251-infected rhesus macaque model. *J. Virol.*
1204 **95**, (2021).
1205 114. Plaza-Jennings, A. L. *et al.* HIV integration in the human brain is linked to microglial
1206 activation and 3D genome remodeling. *Mol. Cell* **82**, 4647-4663.e8 (2022).
1207 115. Morgello, S. *et al.* The National NeuroAIDS Tissue Consortium: a new paradigm in brain
1208 banking with an emphasis on infectious disease. *Neuropathol. Appl. Neurobiol.* **27**, 326–335
1209 (2001).
1210 116. Morgello, S. Chapter 2 - HIV neuropathology. in *Handbook of Clinical Neurology* (ed. Brew,
1211 B. J.) vol. 152 3–19 (Elsevier, 2018).
1212 117. Schlachetzki, J. C. *et al.* Gene expression and chromatin conformation of microglia in virally
1213 suppressed people with HIV. *Life Sci Alliance* **7**, (2024).
1214 118. Riggs, P. K. *et al.* Lessons for Understanding Central Nervous System HIV Reservoirs from
1215 the Last Gift Program. *Curr. HIV/AIDS Rep.* **19**, 566–579 (2022).
1216 119. Alvarez-Carbonell, D. *et al.* Cross-talk between microglia and neurons regulates HIV
1217 latency. *PLoS Pathog.* **15**, e1008249 (2019).
1218 120. Wang, G.-J. *et al.* Decreased brain dopaminergic transporters in HIV-associated dementia
1219 patients. *Brain* **127**, 2452–2458 (2004).
1220 121. Chang, L. *et al.* Decreased brain dopamine transporters are related to cognitive deficits in
1221 HIV patients with or without cocaine abuse. *Neuroimage* **42**, 869–878 (2008).

1222 122. Quizon, P. M. *et al.* Molecular mechanism: the human dopamine transporter histidine 547
1223 regulates basal and HIV-1 Tat protein-inhibited dopamine transport. *Sci. Rep.* **6**, 39048
1224 (2016).
1225 123. Gaskill, P. J., Miller, D. R., Gamble-George, J., Yano, H. & Khoshbouei, H. HIV, Tat and
1226 dopamine transmission. *Neurobiol. Dis.* **105**, 51–73 (2017).
1227 124. Hasin, D. S. *et al.* Psychiatric Research Interview for Substance and Mental Disorders
1228 (PRISM): reliability for substance abusers. *Am. J. Psychiatry* **153**, 1195–1201 (1996).
1229 125. Nelson, C. The Composite International Diagnostic Interview (CIDI) web site. *Bull. World*
1230 *Health Organ.* **77**, 614–614 (1999).
1231 126. Jacobs, M. M., Murray, J., Byrd, D. A., Hurd, Y. L. & Morgello, S. HIV-related cognitive
1232 impairment shows bi-directional association with dopamine receptor DRD1 and DRD2
1233 polymorphisms in substance-dependent and substance-independent populations. *J.*
1234 *Neurovirol.* **19**, 495–504 (2013).
1235 127. Guo, Y. *et al.* Illumina human exome genotyping array clustering and quality control. *Nat.*
1236 *Protoc.* **9**, 2643–2662 (2014).
1237 128. Zhao, S. *et al.* Strategies for processing and quality control of Illumina genotyping arrays.
1238 *Brief. Bioinform.* **19**, 765–775 (2018).
1239 129. Das, S. *et al.* Next-generation genotype imputation service and methods. *Nat. Genet.* **48**,
1240 1284–1287 (2016).
1241 130. Taliun, D. *et al.* Sequencing of 53,831 diverse genomes from the NHLBI TOPMed Program.
1242 *bioRxiv* 563866 (2019) doi:10.1101/563866.
1243 131. Fuchsberger, C., Abecasis, G. R. & Hinds, D. A. minimac2: faster genotype imputation.
1244 *Bioinformatics* **31**, 782–784 (2015).
1245 132. Loh, P.-R. *et al.* Reference-based phasing using the Haplotype Reference Consortium panel.
1246 *Nat. Genet.* **48**, 1443–1448 (2016).

1247 133. Loh, P.-R., Palamara, P. F. & Price, A. L. Fast and accurate long-range phasing in a UK
1248 Biobank cohort. *Nat. Genet.* **48**, 811–816 (2016).
1249 134. Danecek, P. *et al.* Twelve years of SAMtools and BCFtools. *Gigascience* **10**, (2021).
1250 135. Interpreting Intronic and Antisense Reads in 10x Genomics Single Cell Gene Expression
1251 Data - Official 10x Genomics Support. *10x Genomics*
1252 https://www.10xgenomics.com/support/single-cell-gene-
1253 expression/documentation/steps/sequencing/interpreting-intronic-and-antisense-reads-in-10-
1254 x-genomics-single-cell-gene-expression-data.
1255 136. Interpreting Single Cell Gene Expression Data With and Without Intronic Reads - Official
1256 10x Genomics Support. *10x Genomics* https://www.10xgenomics.com/support/single-cell-
1257 gene-expression/documentation/steps/sequencing/interpreting-single-cell-gene-expression-
1258 data-with-and-without-intronic-reads.
1259 137. León-Rivera, R., Morsey, B., Niu, M., Fox, H. S. & Berman, J. W. Interactions of
1260 Monocytes, HIV, and ART Identified by an Innovative scRNAseq Pipeline: Pathways to
1261 Reservoirs and HIV-Associated Comorbidities. *MBio* **11**, (2020).
1262 138. Fleming, S. J. *et al.* Unsupervised removal of systematic background noise from droplet-
1263 based single-cell experiments using CellBender. *bioRxiv* 791699 (2022) doi:10.1101/791699.
1264 139. FireCloud. https://portal.firecloud.org/#methods/cellbender/remove-background/13.
1265 140. Terra. https://app.terra.bio/.
1266 141. Voss, K., Gentry, J. & Van der Auwera, G. Full-stack genomics pipelining with GATK4 +
1267 WDL + Cromwell. (2017) doi:10.7490/f1000research.1114631.1.
1268 142. Virshup, I., Rybakov, S., Theis, F. J., Angerer, P. & Alexander Wolf, F. anndata: Annotated
1269 data. *bioRxiv* 2021.12.16.473007 (2021) doi:10.1101/2021.12.16.473007.
1270 143. Wolock, S. L., Lopez, R. & Klein, A. M. Scrublet: Computational Identification of Cell
1271 Doublets in Single-Cell Transcriptomic Data. *Cell Syst* **8**, 281-291.e9 (2019).

1272 144. Wolf, F. A., Angerer, P. & Theis, F. J. SCANPY: large-scale single-cell gene expression data
1273 analysis. *Genome Biol.* **19**, 1–5 (2018).
1274 145. McInnes, L., Healy, J., Saul, N. & Großberger, L. UMAP: Uniform Manifold Approximation
1275 and Projection. *J. Open Source Softw.* **3**, 861 (2018).
1276 146. Becht, E. *et al.* Dimensionality reduction for visualizing single-cell data using UMAP. *Nat.*
1277 *Biotechnol.* (2018) doi:10.1038/nbt.4314.
1278 147. Korsunsky, I. *et al.* Fast, sensitive and accurate integration of single-cell data with Harmony.
1279 *Nat. Methods* **16**, 1289–1296 (2019).
1280 148. Ianevski, A., Giri, A. K. & Aittokallio, T. Fully-automated and ultra-fast cell-type
1281 identification using specific marker combinations from single-cell transcriptomic data. *Nat.*
1282 *Commun.* **13**, 1246 (2022).
1283 149. Puvogel, S. *et al.* Single-nucleus RNA sequencing of midbrain blood-brain barrier cells in
1284 schizophrenia reveals subtle transcriptional changes with overall preservation of cellular
1285 proportions and phenotypes. *Mol. Psychiatry* **27**, 4731–4740 (2022).
1286 150. Tiklová, K. *et al.* Single-cell RNA sequencing reveals midbrain dopamine neuron diversity
1287 emerging during mouse brain development. *Nat. Commun.* **10**, 581 (2019).
1288 151. Fang, Z., Liu, X. & Peltz, G. GSEApy: a comprehensive package for performing gene set
1289 enrichment analysis in Python. *Bioinformatics* **39**, (2023).
1290 152. Ashburner, M. *et al.* Gene ontology: tool for the unification of biology. The Gene Ontology
1291 Consortium. *Nat. Genet.* **25**, 25–29 (2000).
1292 153. Gene Ontology Consortium *et al.* The Gene Ontology knowledgebase in 2023. *Genetics* **224**,
1293 (2023).
1294 154. Subramanian, A. *et al.* Gene set enrichment analysis: a knowledge-based approach for
1295 interpreting genome-wide expression profiles. *Proc. Natl. Acad. Sci. U. S. A.* **102**, 15545–
1296 15550 (2005).

155. Mootha, V. K. *et al.* PGC-1alpha-responsive genes involved in oxidative phosphorylation are coordinately downregulated in human diabetes. *Nat. Genet.* **34**, 267–273 (2003).

156. Agarwal, D. *et al.* A single-cell atlas of the human substantia nigra reveals cell-specific pathways associated with neurological disorders. *Nat. Commun.* **11**, 4183 (2020).

Acknowledgments

General: We thank the staff and patients of the Manhattan HIV Brain Bank; this research would not be possible without their valuable contributions. We also thank all members of the Single Cell Opioid Responses in the Context of HIV (SCORCH) consortium for stimulating and helpful discussions, and Roger Pique-Regi for guidance on demuxlet software. This work was supported in part through the computational and data resources provided by the Scientific Computing and Data Center at Icahn School of Medicine at Mount Sinai. The content is solely the responsibility of the authors and does not necessarily represent the official views of the National Institutes of Health.

Funding: This work was supported by
National Institutes of Health grant U01DA053600 (SA, SM)
National Institutes of Health grant R61DA048207 (SA, SM)
National Institutes of Health grant R01NS108801 (SM)
National Institutes of Health grant RFAG060961 (SM)
National Institutes of Health grant U24MH100931 (SM)
National Institutes of Health contract 75N95023C00015 (SM)
National Institutes of Health Office of Research Infrastructure grant S10OD026880 (Patricia Kovach, ISMMS)
National Institutes of Health Office of Research Infrastructure grant S10OD030463 (Patricia Kovach, ISMMS)
National Center for Advancing Translational Sciences Clinical and Translational Science Awards grant UL1TR004419 (Rosalind Wright, ISMMS)

Author contributions:
Conceptualization: SA, SM
Methodology: AW, MJ, SA, SM
Software: AW
Validation: AW, MJ, AV, TL, SA, SM
Formal analysis: AW
Investigation: AW, MJ, GM, EG, JM, AV, TL, SM
Resources: SA, SM
Data curation: AW, MJ, AV, TL, SM
Writing—original draft: AW
Writing—review & editing: AW, MJ, SA, SM
Visualization: AW
Supervision: AW, MJ, GM, SA, SM
Project administration: SA, SM
Funding acquisition: SA, SM

Competing interests:

The authors declare that they have no competing interests.

Data and materials availability:

All data needed to evaluate the conclusions in the paper are present in the paper and/or the Supplementary Materials. Data presented in this study were produced as part of the Single Cell Opioid Response in the Context of HIV consortium (SCORCH: RRID:SCR_022600). De-identified snRNA-seq data, donor SNP arrays, and associated metadata will be deposited at dbGaP (https://www.ncbi.nlm.nih.gov/gap/) and made available prior to publication. The data at dbGaP is controlled-access and requires special handling; please follow dbGaP guidelines and contact dbGaP for support. Mapped, demultiplexed snRNA-seq data will also be made publicly available at the NEMO (Neuroscience Multi-omic) Archive under identifier nemo:dat-zngw2c8 (https://assets.nemoarchive.org/dat-zngw2c8) prior to publication. Code used to perform the analyses in this paper will be made publicly available on Github and Zenodo prior to publication.

1359 **Figures and Tables**

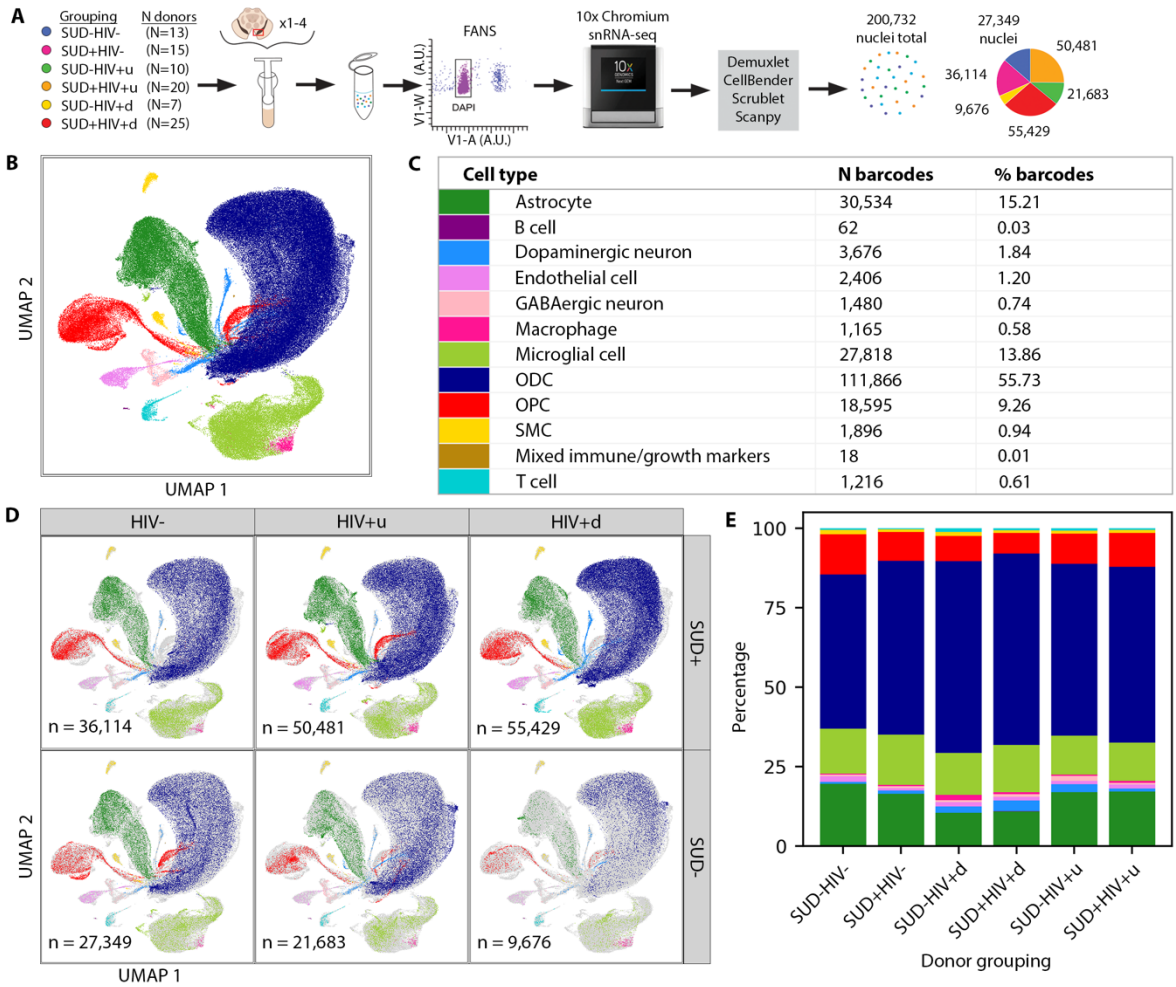

1360
1361 **Fig. 1. snRNA-seq data generation and cell typing results. (A)** Schematic of study
1362 design and snRNA-seq data acquisition procedure (showing at left the number of
1363 donors per study group and at right, with the same color-coding, each group's final
1364 number of QC-passing nuclei). "V1-W" and "V1-A": width and area, respectively,
1365 of violet-channel fluorescence signal used for detecting intact nuclei with
1366 fluorescence-activated nuclear sorting (FANS); "DAPI": 4′,6-diamidino-2-
1367 phenylindole. **(B)** 2D UMAP showing the cell types we identified, with cell type
1368 colors as shown in **(C)**. **(C)** Numbers and fractions of nuclei of each cell type. **(D)**
1369 UMAPs showing nuclei by cell type for each donor group (colors as in **(C)**). **(E)**
1370 Cell type proportions for each donor group (see also Table S5), with colors as
1371 shown in **(C)**: red, oligodendrocyte precursor cells (OPC); dark blue,
1372 oligodendrocytes (ODC); light green, microglia; dark green, astrocytes; and less-
1373 frequent cell types including in light blue, DA neurons and rose, GABA neurons.

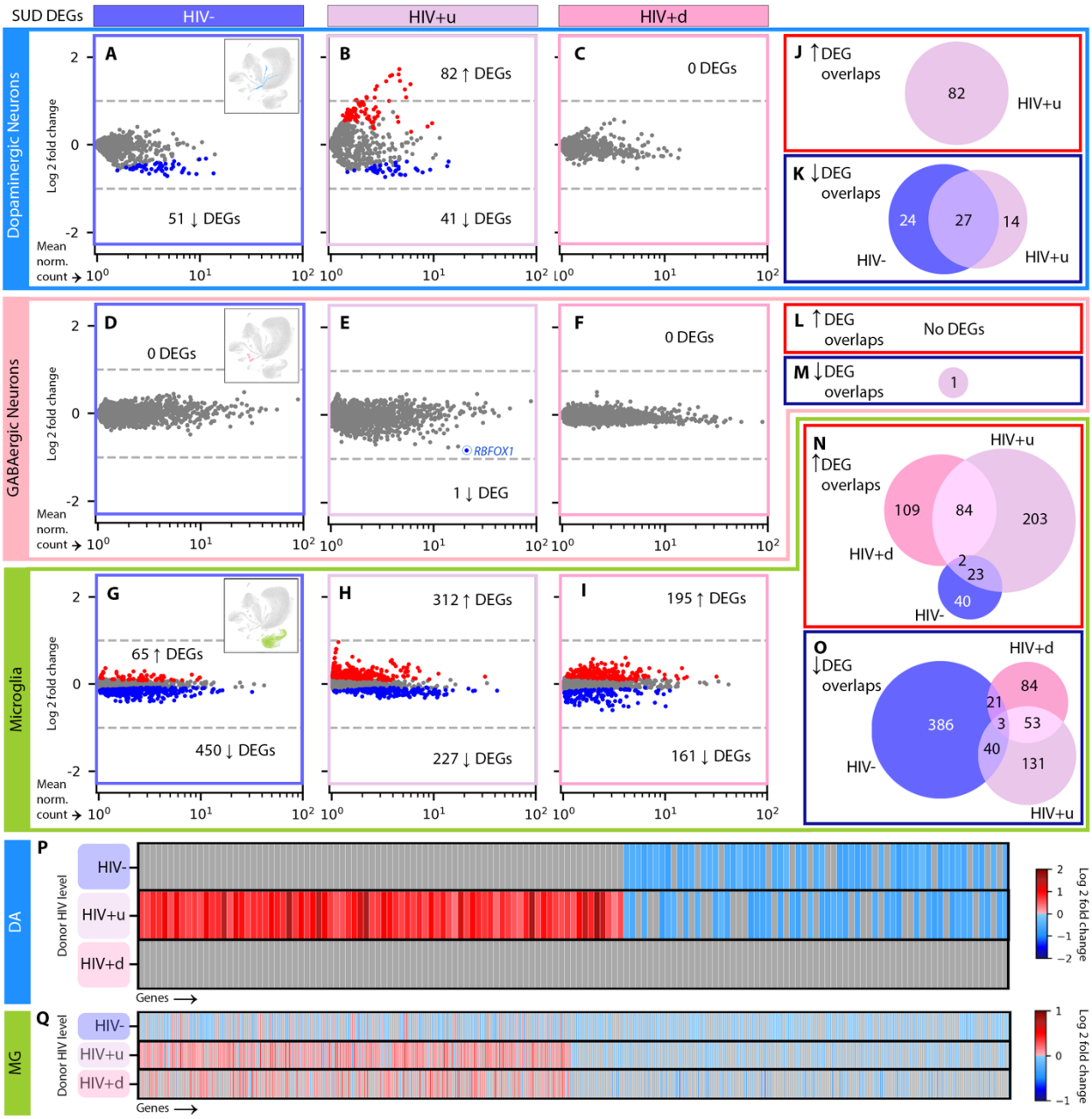

Fig. 2. SUD-attributed DEGs by cell type. (A)-(C) SUD DEGs in DA neurons of **(A)** HIV- (dark purple), **(B)** HIV+u (light purple), and **(C)** HIV+d (pink) donors. Red and blue dots: significantly up- and down- regulated DEGs, respectively ($p < 0.05$). Numbers of up- and down- DEGs are shown. **(D)-(F):** SUD DEGs in GABA neurons for **(D)** HIV-, **(E)** HIV+u, and **(F)** HIV+d donors. In **(E)**, the DEG *RBFOX1* is circled. **(G)-(I)** SUD DEGs in microglia for **(G)** HIV-, **(H)** HIV+u, and **(I)** HIV+d donors. **(J)-(O)** Venn diagrams showing the extent of overlap among SUD DEGs across HIV levels for **(J)** DA neuron up- and **(K)** down- DEGs; **(L)** GABA neuron up- and **(M)** down- DEGs; and **(N)** microglia up- and **(O)** down-DEGs. **(P)-(Q)** Gene-by-gene comparisons of differential transcription across HIV levels for **(P)** DA neurons and **(Q)** microglia. Columns in **(P)**, **(Q)** contain all genes arising as SUD DEGs at any HIV level; rows correspond to HIV levels. Genes per HIV level (row) are colored by log2 fold change (l2fc) if they are DEGs (see color bar) or gray if not. DA neuron, GABA neuron, and microglial nuclei are shown in the UMAP insets in **(A)**, **(D)**, and **(G)**, respectively.

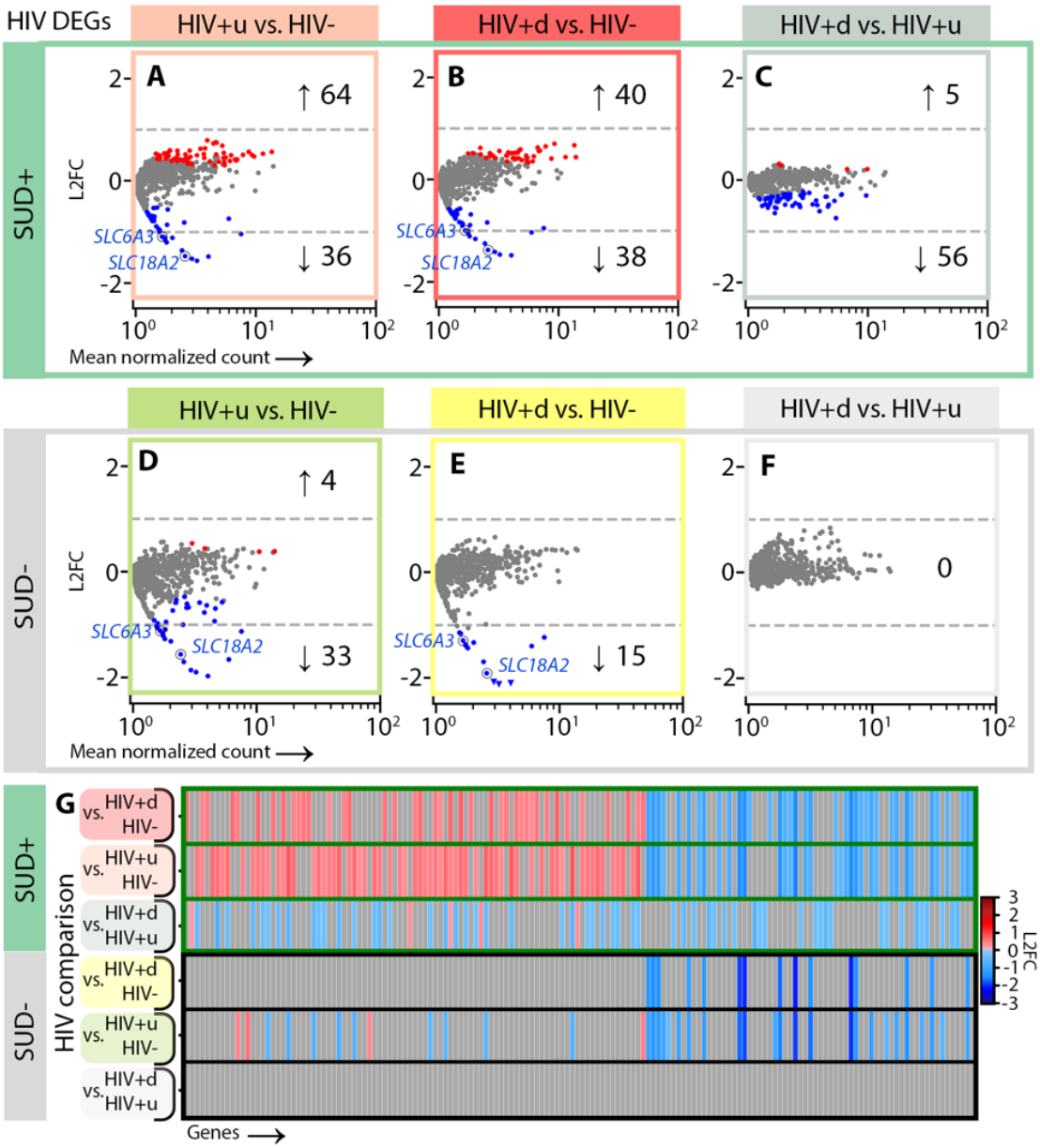

Fig. 3. HIV-attributed DEGs for DA neurons. (A)-(C) HIV DEGs occurring in SUD+ individuals ($p < 0.05$) for DA neurons, for DEAs of **(A)** SUD+HIV+u vs. SUD+HIV- (peach), **(B)** SUD+HIV+d vs. SUD+HIV- (red), and **(C)** SUD+HIV+d vs. SUD+HIV+u (gray). **(D)-(F)** HIV DEGs occurring in SUD- individuals for DEAs of **(D)** SUD-HIV+u vs. SUD-HIV- (green), **(E)** SUD-HIV+d vs. SUD-HIV- (yellow), and **(F)** SUD-HIV+d vs. SUD-HIV+u (gray). **(G)** Gene-by-gene comparisons of differential transcription across HIV comparisons for (top 3 rows) SUD+ and (bottom 3 rows) SUD-, similar to **Figs. 2P**, **Q**. In **(A)**, **(B)**, **(D)**, and **(E)**, monoamine transporter DEGs *SLC6A3* and *SLC18A2* are circled.

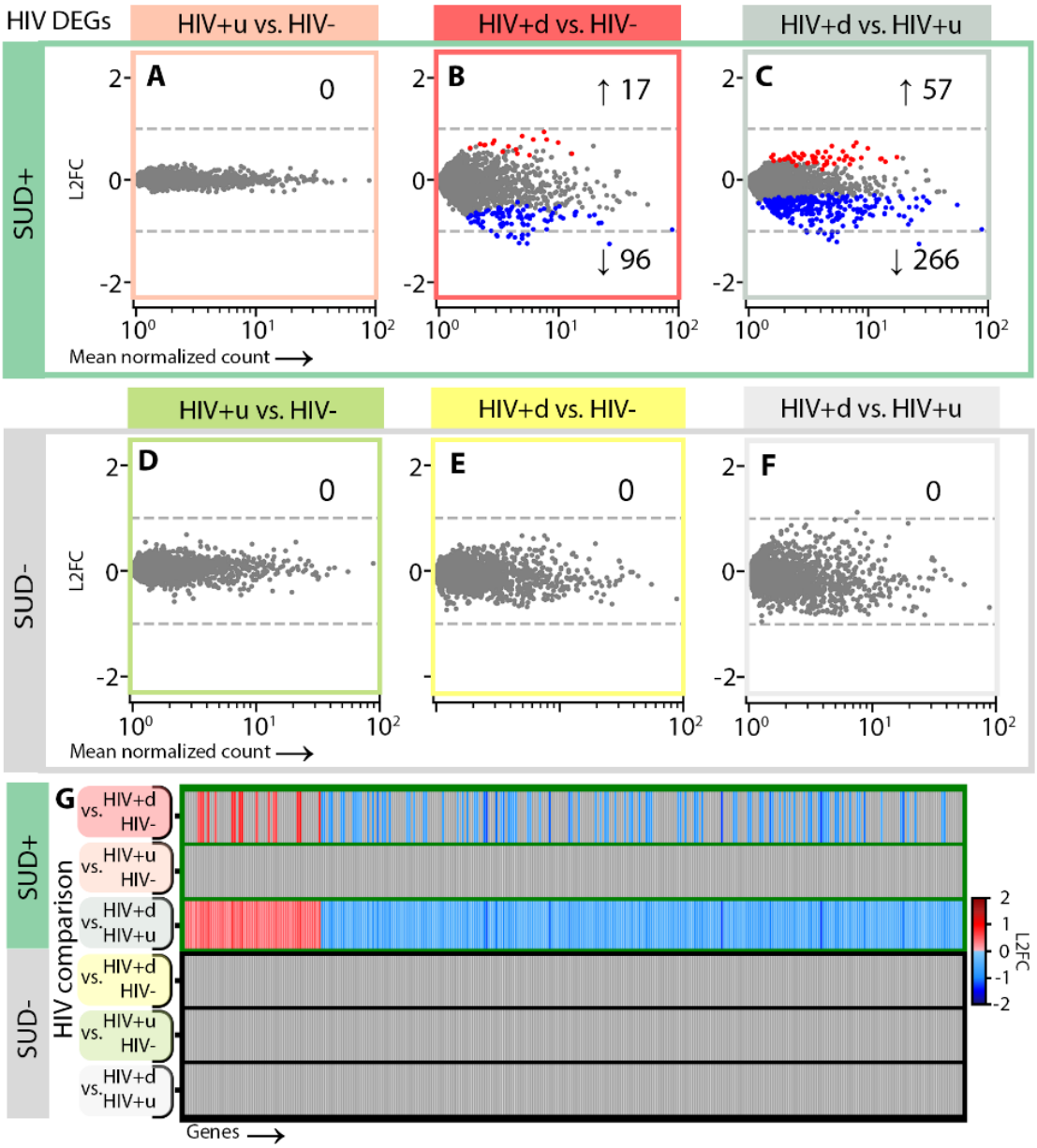

Fig. 4. HIV-attributed DEGs for GABA neurons. (A)-(C) HIV DEGs ($p < 0.05$) for GABA neurons in SUD+ donors, for DEAs of **(A)** SUD+HIV+u vs. SUD+HIV- (peach), **(B)** SUD+HIV+d vs. SUD+HIV- (red), and **(C)** SUD+HIV+d vs. SUD+HIV+u (gray). **(D)-(F)** HIV DEGs in SUD- donors for **(D)** SUD-HIV+u vs. SUD-HIV- (green), **(E)** SUD-HIV+d vs. SUD-HIV- (yellow), and **(F)** SUD-HIV+d vs. SUD-HIV+u (gray). **(G)** Gene-by-gene comparisons of differential transcription across HIV comparisons for SUD+ and SUD- donors.

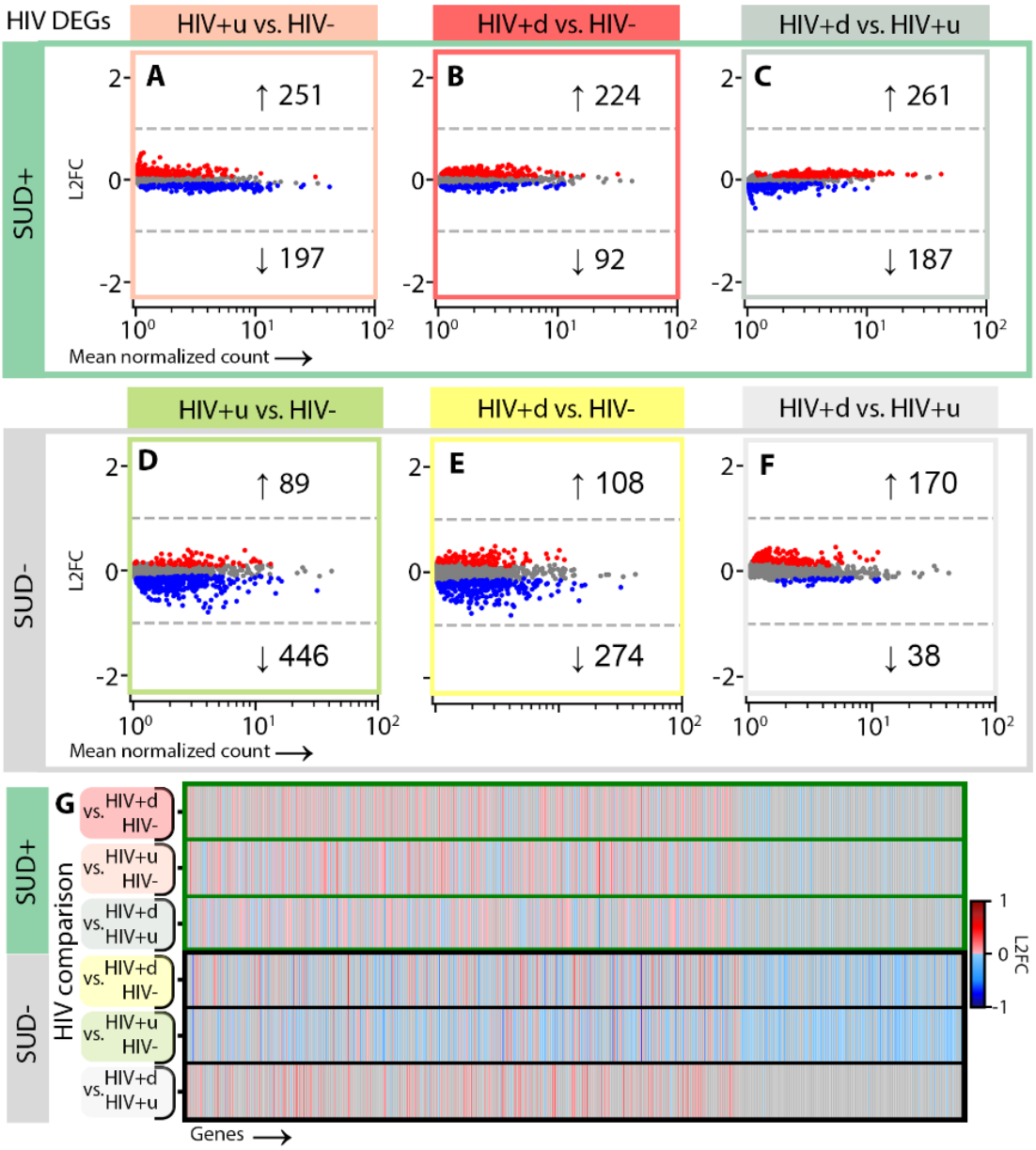

Fig. 5. HIV-attributed DEGs for microglia. (A)-(C) HIV DEGs ($p < 0.05$) for microglia in SUD+ donors for DEAs of **(A)** SUD+HIV+u vs. SUD+HIV- (peach), **(B)** SUD+HIV+d vs. SUD+HIV- (red), and **(C)** SUD+HIV+d vs. SUD+HIV+u (gray). **(D)-(F)** HIV DEGs in SUD- donors for DEAs of **(D)** SUD-HIV+u vs. SUD-HIV- (green), **(E)** SUD-HIV+d vs. SUD-HIV- (yellow), and **(F)** SUD-HIV+d vs. SUD-HIV+u (gray). **(G)** Gene-by-gene comparisons of differential transcription across HIV comparisons for SUD+ and SUD- donors.

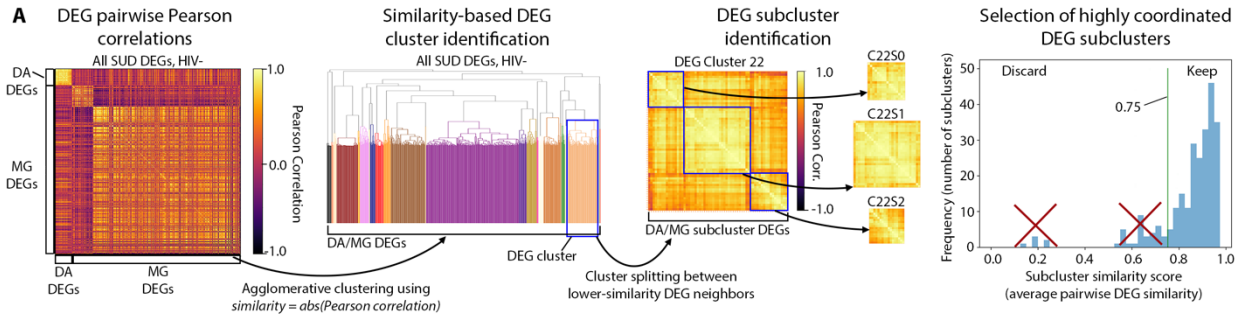

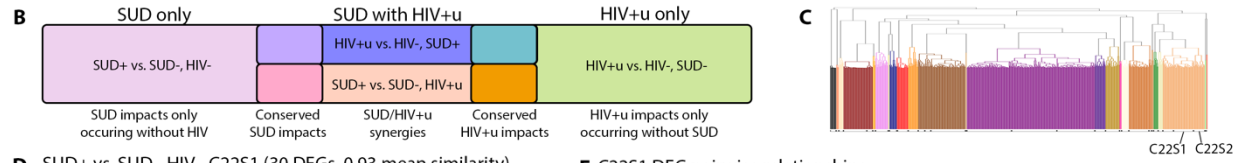

D SUD+ vs. SUD-, HIV-, C22S1 (30 DEGs, 0.93 mean similarity)

Cell type	Functional group	DEGs
Microglial Cells	Enhanced microglial activation	*FUT8*↓
Dopaminergic Neurons	**Impaired membrane, axon, dendrite maintenance**	*SEPTIN7*↓, *FUT8*↓, *ENPP2*↓, ***TTLL7***↓, *DOCK4*↓, ***SLAIN1***↓, ***CLMN***↓, ***ZNF536***↓, *SPOCK3*↓
	Altered postsynaptic machinery	***PLCG2***↓, ***EDIL3***↓, *PKP4*↓, *DLG1*↓, ***ERBIN***↓, ***PLCL1***↓
	Increased neuronal excitability, presynaptic release	***GRM3***↓, ***KCNH8***↓, ***PDE1C***↓, *SH3GL3*↓
	Reduced presynaptic release frequency	***ATP8A1***↓
	Increased excitability, senescence-like signaling	*SAMD12*↓
	Buildup of cytotoxic compounds	***TMEM144***↓, ***TF***↓, *OTUD7A*↓, ***KLHL32***↓, ***DPYD***↓, ***TMTC2***↓
	Disinhibition of neuroprotective signaling	*HHIP*↓
	Decreased neuron survival	*TMEFF2*↓

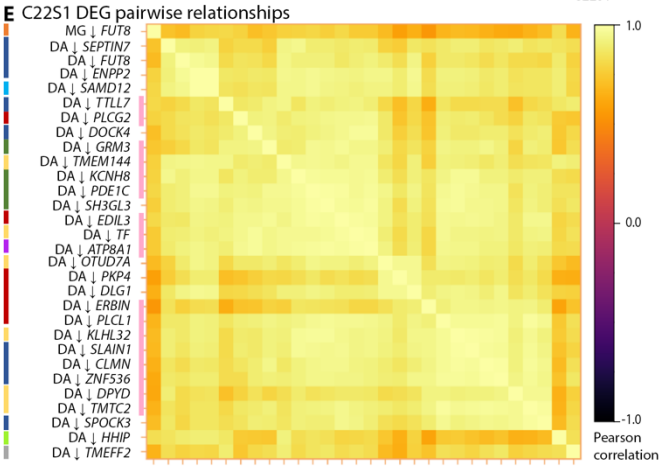

F SUD+ vs. SUD-, HIV-, C22S2 (17 DEGs, 0.90 mean similarity)

Cell type	Functional group	DEGs
Microglial Cells	Activation-associated alterations in metabolism	*MT-CO3*↓, *MT-ND4*↓, *MT-CYB*↓, *MT-CO1*↓, *MCU*↓
	Reduced anti -viral/-bacterial response capability	*FGF12*↓, *EDA*↓, *EIF2AK2*↓, *SAMD9L*↓, *IFI44*↓, *MX1*↓, *PARP14*↓
	Disinhibition of senescence-like signaling	*XAF1*↓
	Reduced neuronal maintenance/protection	*MTRNR2L12*↓
	Potentially enhanced neuronal/synaptic interactions	*MDGA2*↓, *SPATS2L*↓
Dopaminergic Neurons	Impaired presynaptic signal transduction and reuptake	***GPM6B***↓

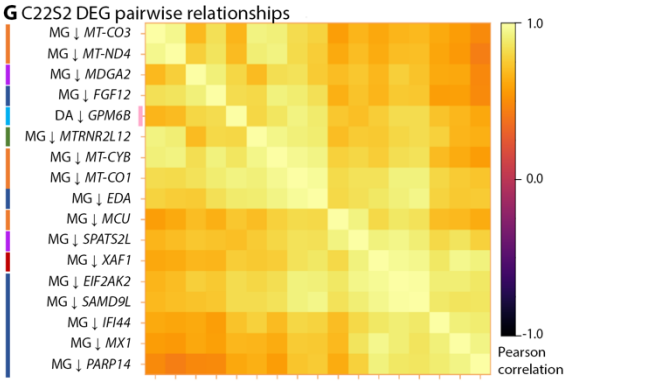

Fig. 6. DEG subclustering approach and DA neuron/microglial DEG subclusters showing SUD impacts. (A) Schematic of our approach for identifying DEG subclusters, for DA neuron (DA) and microglial (MG) DEGs, for the DEA comparing SUD+HIV- vs. SUD-HIV- (Methods). **(B)** Venn diagram showing interpretations for DEG subcluster functions based on the DEAs they arise in, for the 4 DEAs assessing impacts of SUD (left, **Figs. 2A, G**), HIV+u (right, **Figs. 3D, 5D**), or SUD+HIV+u (middle, **Figs. 2B, H**, **3A, 5A**). **(C)** Dendrogram for DEGs from SUD+HIV- vs. SUD-HIV-, showing subclusters for SUD impacts. Labels denote subclusters shown in **(D)-(G)**. **(D)** Subcluster C22S1 DEGs, organized by functional group (indexed by color at right). Fill color follows the legend in **(B)**; bold denotes DEGs recurring as SUD impacts in SUD+HIV+u donors. **(E)** Heatmap showing pairwise DEG correlations for subcluster C22S1, with DEG names colored by functional group to left and pink to right if recurring in SUD+HIV+u. **(F)**, **(G)** Similar to **(D)**, **(E)**, but for subcluster C22S2.

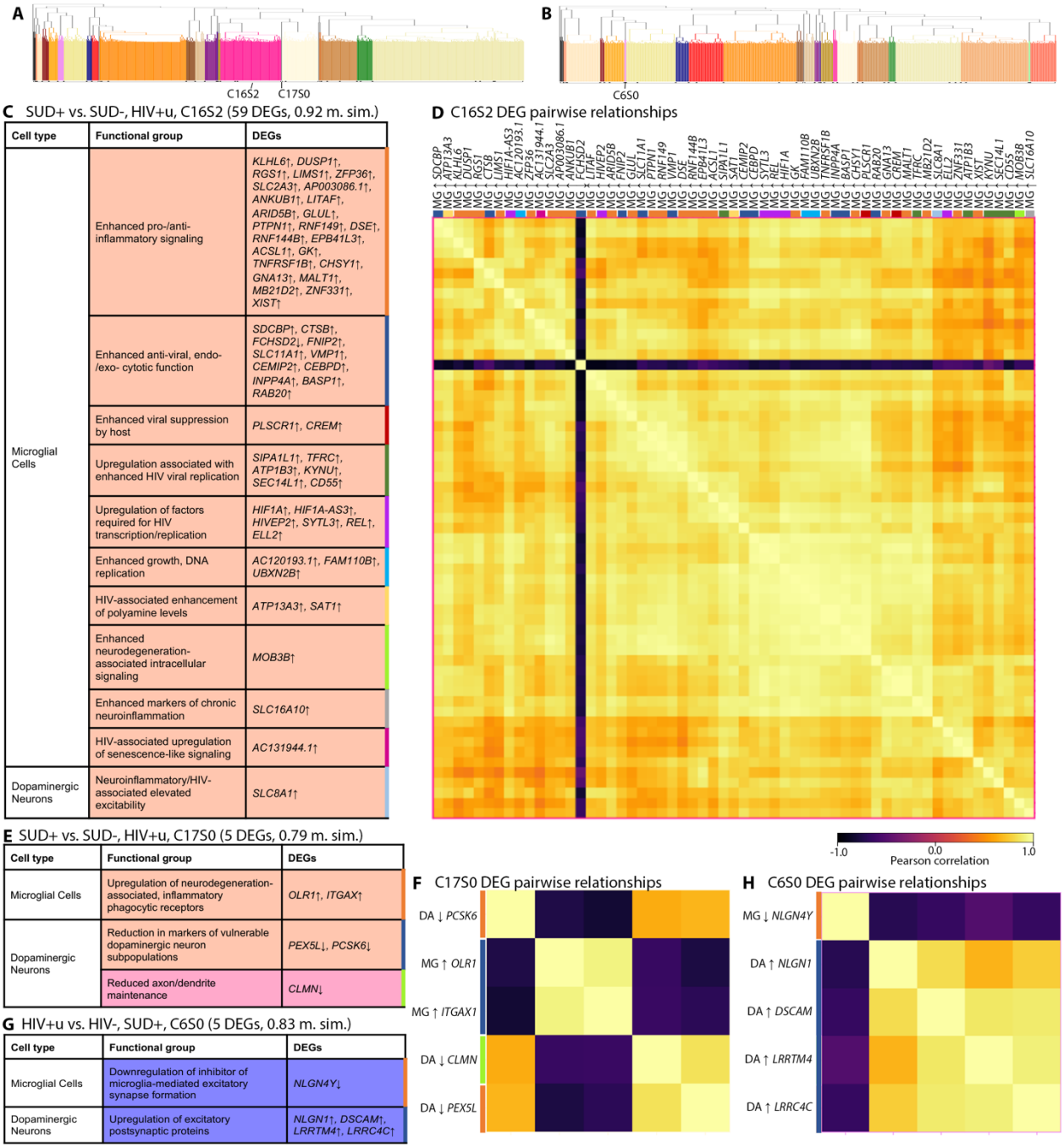

Fig. 7. DA neuron/microglial DEG subclusters showing added functional impacts for SUD+HIV+u donors. (A) Dendrogram relating DA/MG DEGs for the comparison of SUD+HIV+u vs. SUD-HIV+u (**Figs. 2B**, **H**), with labels indicating subclusters shown in **(C)-(F)**. **(B)** Dendrogram relating DEGs for SUD+HIV+u vs. SUD+HIV- (**Figs. 3A**, **5A**), with labels indicating subcluster in **(G)**, **(H)**. **(C)** Subcluster C16S2 DEGs organized by functional group (indexed by color at right); fill color follows the legend in **Fig. 6B** (pink: SUD impacts; orange: impacts specific to SUD+HIV+u dual diagnosis). "m. sim": subcluster mean pairwise similarity. **(D)** Heatmap of pairwise DEG correlations for subcluster C16S2, with DEG names colored by functional group. **(E)**, **(F)** Similar to **(C)**, **(D)** but for subcluster C17S0. **(F)**, **(H)** Similar to **(C)**, **(D)** but for subcluster C6S0.

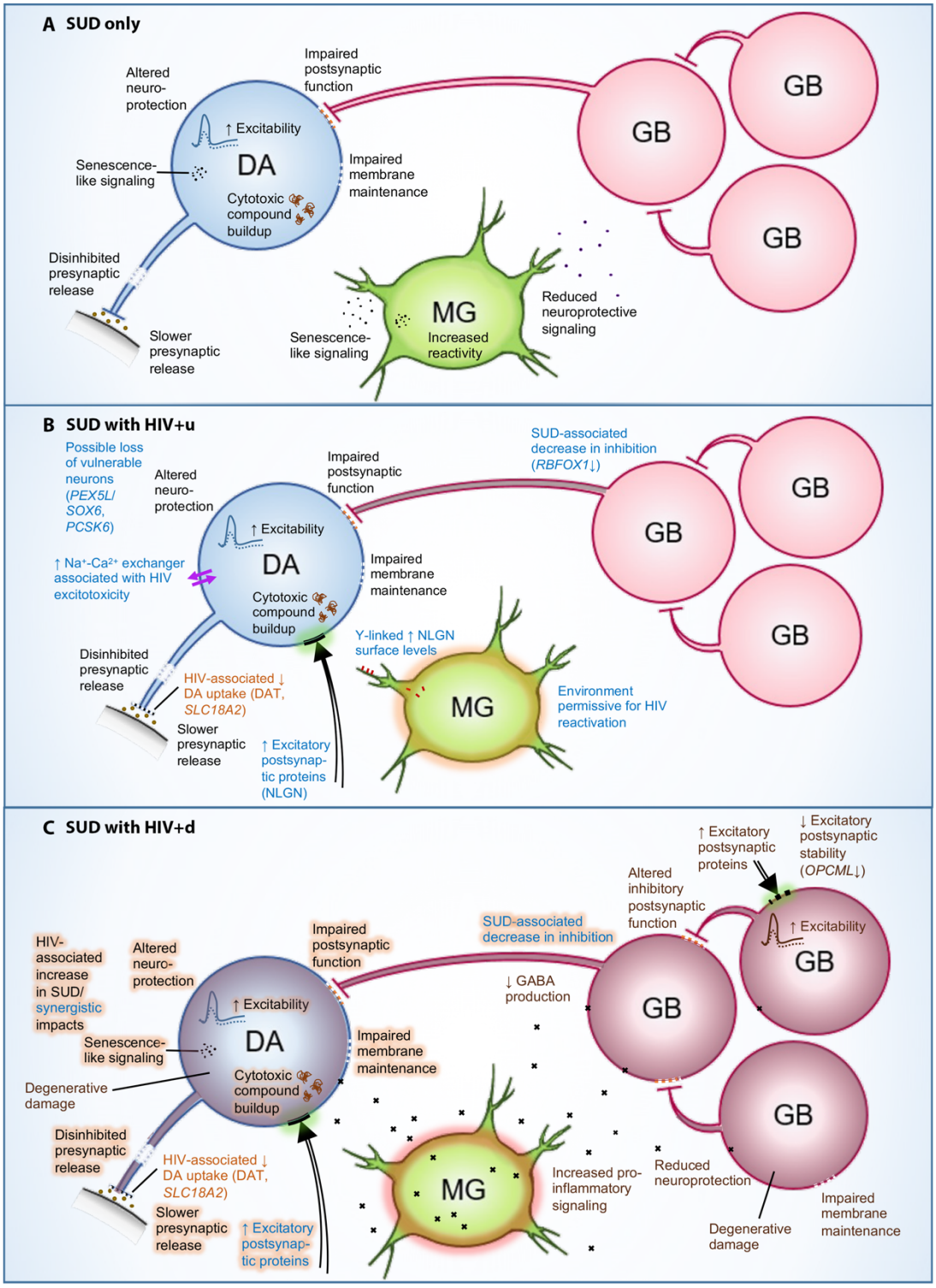

Fig. 8. Summary of functional impacts identified for SUD and HIV. Schematics summarizing the biological impacts identified for **(A)** SUD only, **(B)** SUD with HIV+u, and **(C)** SUD with HIV+d, on DA neurons (blue cells; "DA"), GABA neurons (pink cells; "GB"), and microglia (green cells; "MG"). Descriptions indicate biological impacts, with font color showing DEA-based association with HIV and/or SUD (black: SUD impacts; light brown: HIV+u impacts; blue: HIV+u/SUD+ synergistic impacts; dark brown: HIV+d impacts), and with light brown highlights indicating HIV+d-associated enhancement of impacts.

1460 **Table 1. Demographic characteristics of donor groups.**

	Entire Sample	SUD- HIV- (n=13)	SUD+ HIV- (n=15)	SUD- HIV+u (n=10)	SUD+ HIV+u (n=20)	SUD- HIV+d (n=7)	SUD+ HIV+d (n=25)
Mean (standard deviation) age [years]	54.0 (11.4)	47.5 (2.9)	54.3 (2.7)	60.1 (3.3)	60.8 (2.3)	54.0 (4.0)	49.4 (2.1)
Number (percent) male sex	51 (57%)	7 (54%)	12 (80%)	5 (50%)	10 (50%)	4 (57%)	13 (52%)
Race/ethnicity by number (percent)	34 (38%) Non-Hisp Black 30 (33%) Hisp. 20 (22%) Non-Hisp White 6 (7%) Other	2 (15%) Non-Hisp Black 6(46%) Hisp 3 (23%) Non-Hisp White 2 (15%) Other	4 (27%) Non-Hisp Black 5(33%) Hisp 6 (40%) Non-Hisp White 0 (0%) Other	2 (20%) Non-Hisp Black 2(20%) Hisp 6 (60%) Non-Hisp White 0 (0%) Other	9 (45%) Non-Hisp Black 8(40%) Hisp 1 (5%) Non-Hisp White 2 (10%) Other	3 (43%) Non-Hisp Black 1(14%) Hisp 1 (14%) Non-Hisp White 2 (29%) Other	14 (56%) Non-Hisp Black 8(32%) Hisp 3 (12%) Non-Hisp White 0 (0%) Other
Median (IQR) CD4 T cell count	165 (71, 425)	N/A	N/A	378 (208, 648)	269 (135, 421)	242 (185, 400)	69 (15, 102)
Median (IQR) nadir CD4 T cell count	54 (12, 139)	N/A	N/A	113 (80, 270)	60 (13, 172)	93 (17, 185)	22 (6, 58)
Opioid/ cocaine SUD diagnoses by number	Opioid and cocaine 28 Opioid only 14 Cocaine only 18	N/A	Opioid and cocaine 10 Opioid only 4 Cocaine only 1	N/A	Opioid and cocaine 10 Opioid only 4 Cocaine only 6	N/A	Opioid and cocaine 8 Opioid only 6 Cocaine only 11
Number (percent) with exposure to other substances	67 (74%)	3 (23%)	10(67%)	8 (80%)	19 (95%)	6 (86%)	21 (84%)

1461 Statistical comparisons of donor characteristics across donor groups are provided in Table S2.
1462 Numbers of nuclei by donor group are provided in Table S3.
1463
1464

Supplementary Materials for

Transcriptional impacts of substance use disorder and HIV on human ventral midbrain neurons and microglia

Alyssa Wilson* *et al.*

*Corresponding author. Email: alyssa.wilson@mssm.edu

This PDF file includes:

Figs. S1 to S5
Tables S3, S6, S8

Other Supplementary Materials for this manuscript include the following:

Tables S1, S2, S4, S5, S7
Data S1 to S9

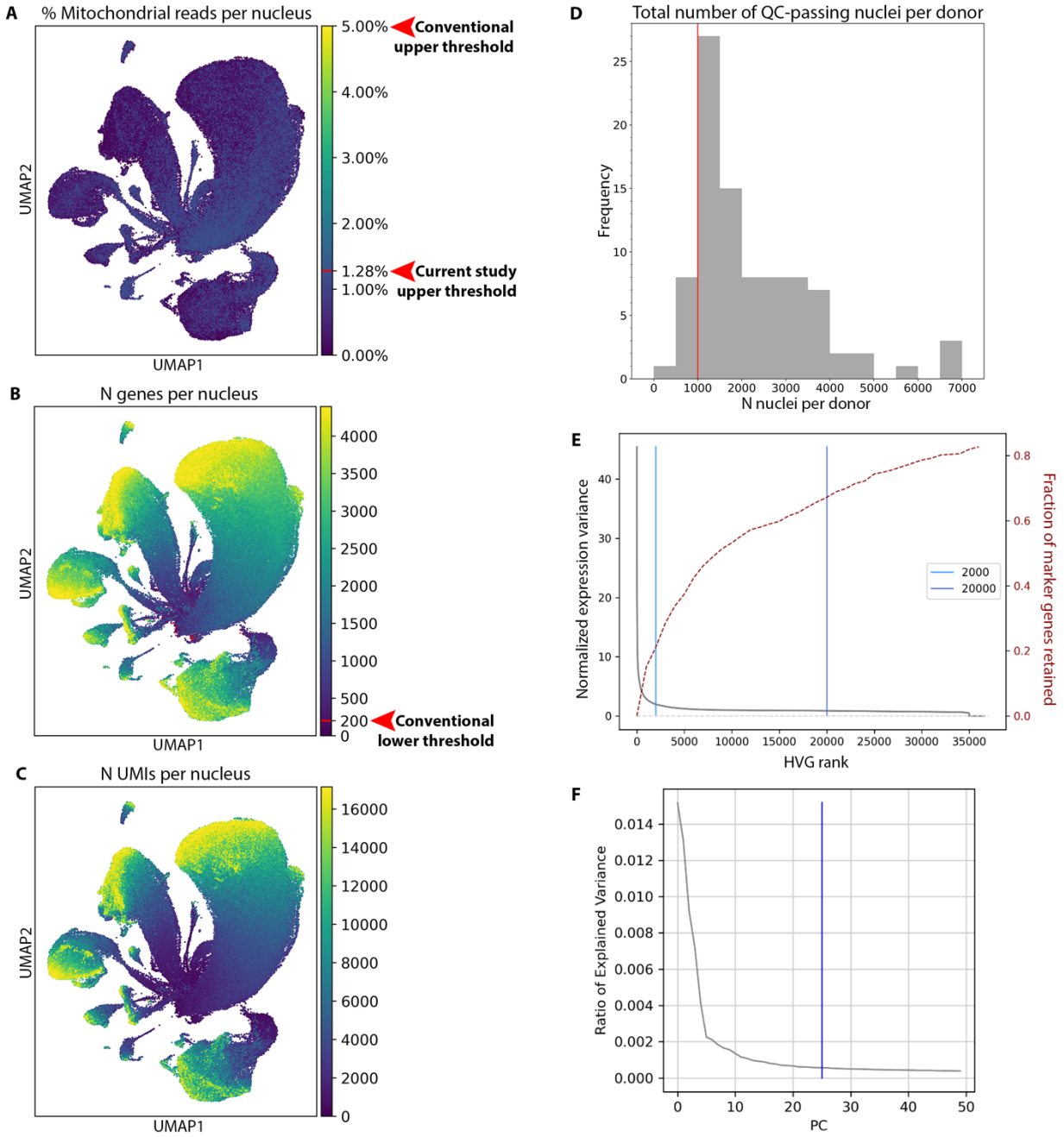

Fig. S1. Additional information about snRNA-seq QC and pre-processing.

(A)-(C) UMAPs showing values of QC heuristics, only for nuclei passing all QC nuclei. **(A)** Percent mitochondrial reads/nucleus. Red line/arrowhead at 1.28% shows the maximum value in our QC-passing nuclei; line at 5% shows a conventional filtering maximum. **(B)** Number of genes/nucleus; red line/arrowhead shows a conventional lower threshold of 200; QC-passing nuclei with <200 genes are colored red (see Fig. S2). **(C)** Number of UMIs/nucleus. **(D)** Distribution of the number of QC-passing nuclei/donor. Red line: the 1,000-nuclei threshold exceeded by 90% of donors. **(E)** Parameters used to determine the number of HVGs retained in analysis. Genes are ranked left to right by decreasing variability; black line (left y-axis) shows each gene's normalized expression variance; red line (right y-axis) shows the fraction of all genes ≤ that rank in our marker gene database. Blue lines show (right) our cutoff (20,000 HVGs) and (left) a conventional one (2,000 HVGs). **(F)** Explained variances of principle component analysis components ("PCs"); blue line shows the maximum component we retained, the 25th PC.

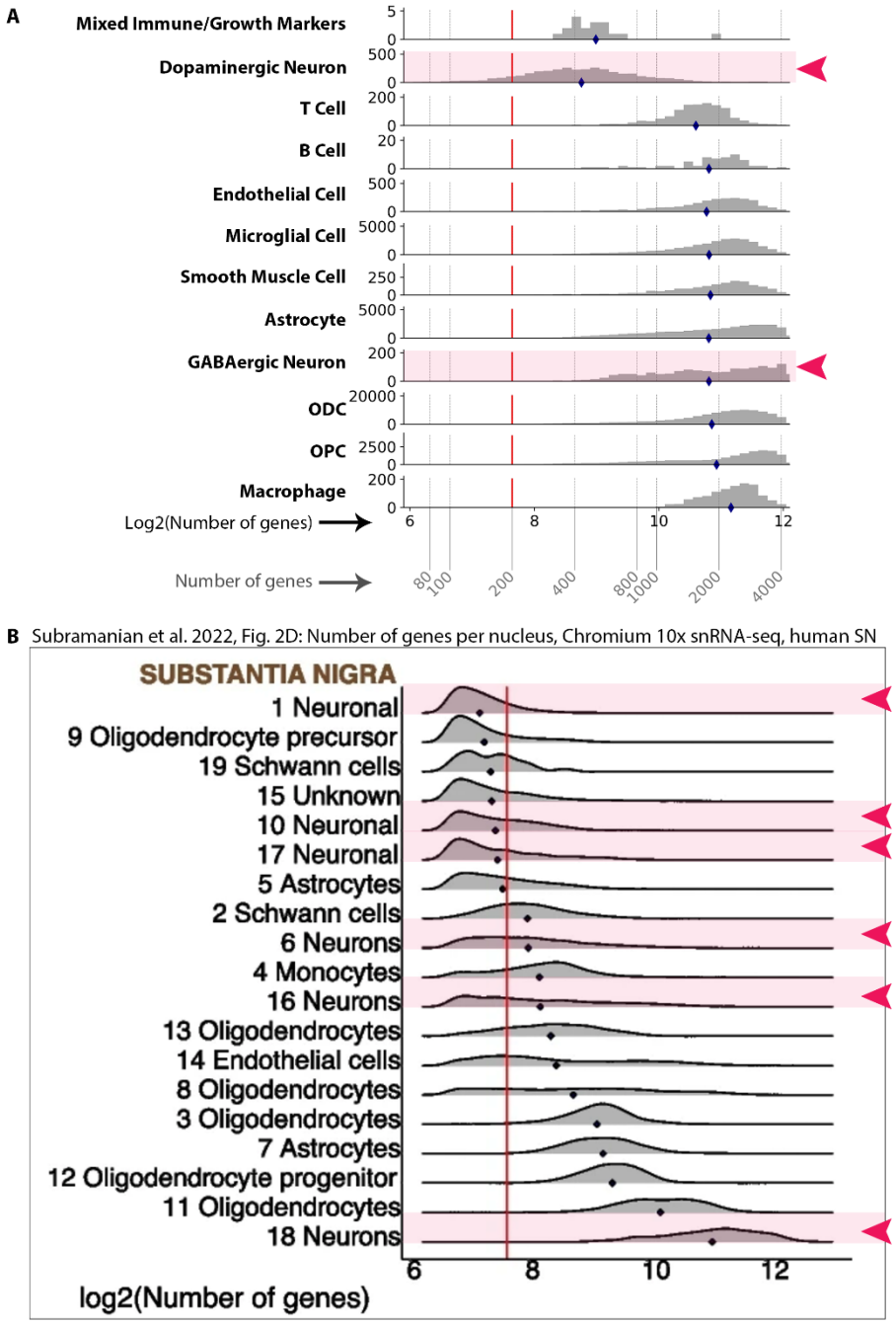

Fig. S2. Comparison of N genes/nucleus, by cell type, to published SN snRNA-seq data. **(A)** Histograms showing the log-transformed number of genes/nucleus, by cell type, for our QC-passing nuclei (**Figs. 1B**, **C**). Gray dashed lines show corresponding raw (non-log-transformed) gene counts. **(B)** Histograms showing log-transformed number of genes/nucleus for each cluster identified in previously published human SN snRNA-seq data, prepared similarly to ours (via Chromium 10x[1]). For **(A)** and **(B)**, neuronal cell types are marked with pink highlights and arrowheads, distribution means are indicated by blue diamonds, and red lines show the conventional lower threshold of 200 genes/nucleus.

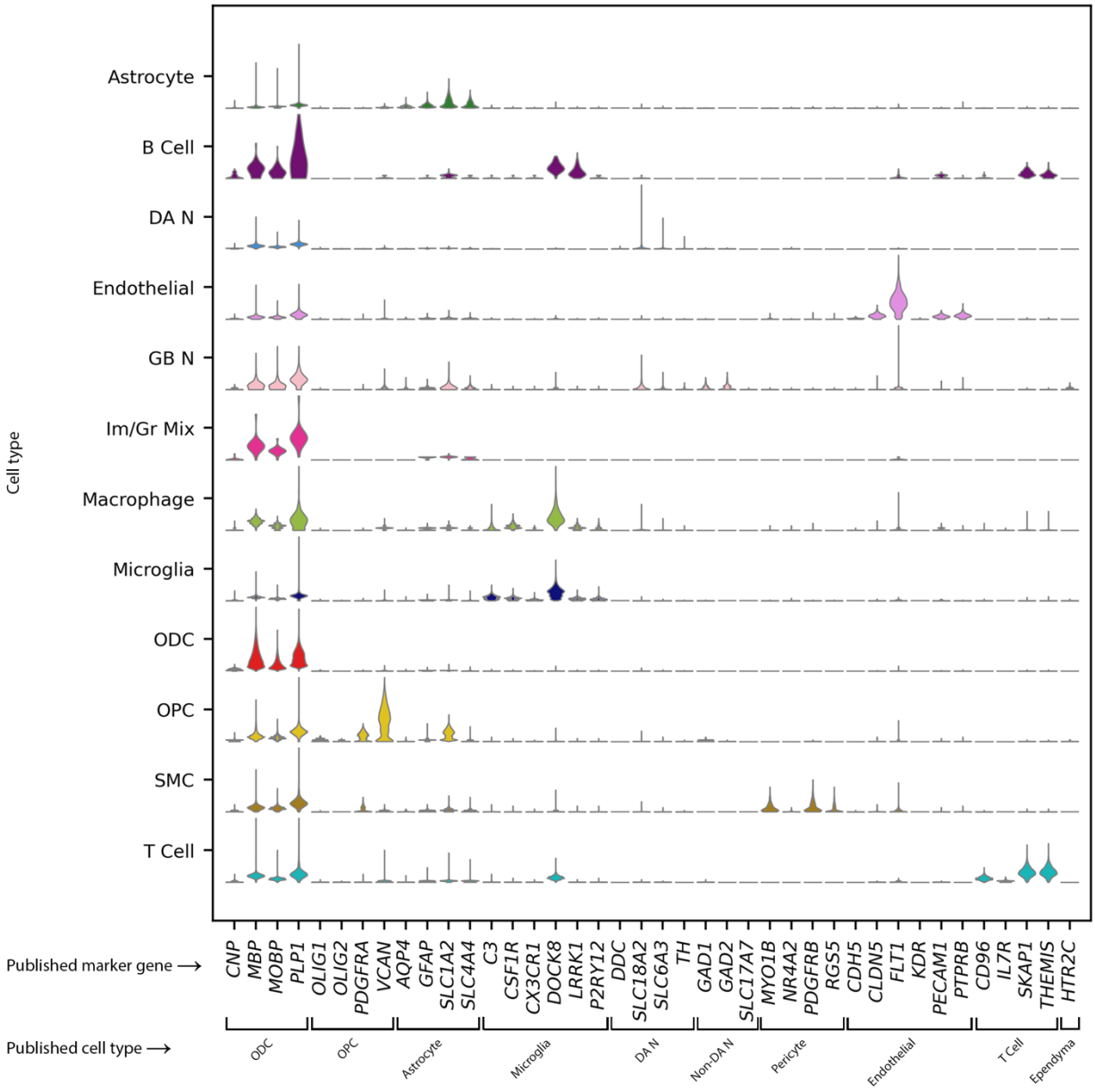

Fig. S3. Expression of previously published SN cell type marker genes, by cell type. Expression in each of our cell types (rows) of previously identified (Wei et al. 2023[2]) marker genes for ventral midbrain cell types (columns).

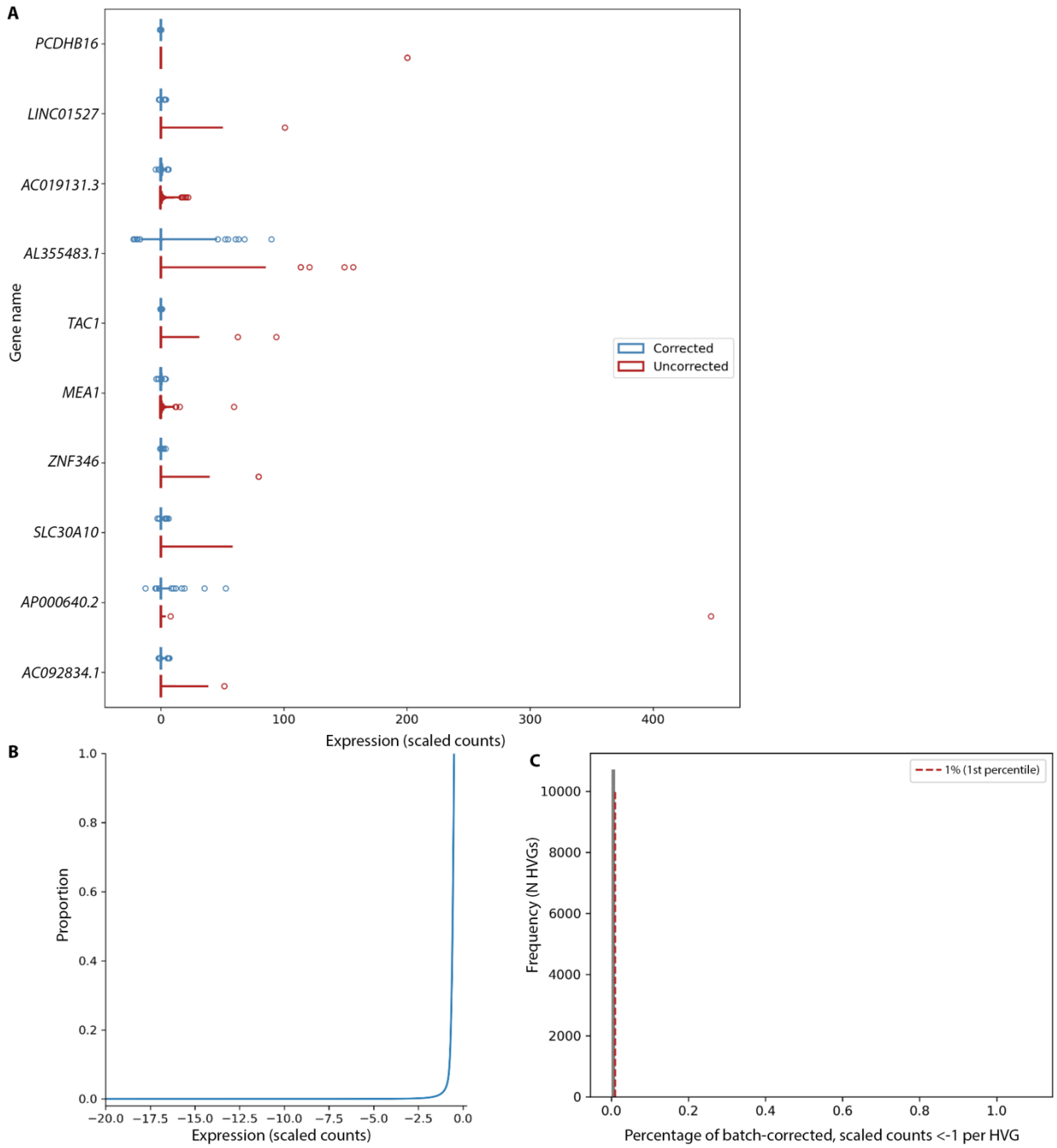

Fig. S4. Impacts of batch correction on gene expression distributions for QCed data. **(A)** Gene expression distributions before (red) vs. after (blue) batch correction, for 10 example HVGs selected randomly from our 20,000. **(B)** An empirical cumulative distribution showing the values of all batch-corrected, still-scaled read counts with values ≤ -0.5 (that would round to non-negligible negative counts ≤-1), highlighting a vanishing number of counts shifted to values <-2 by batch correction. **(C)** Distribution showing the percentages of each HVG's batch-corrected counts with values <-1. Red line denotes 1% (corresponding to the lowest 1st percentile of an HVG's distribution).

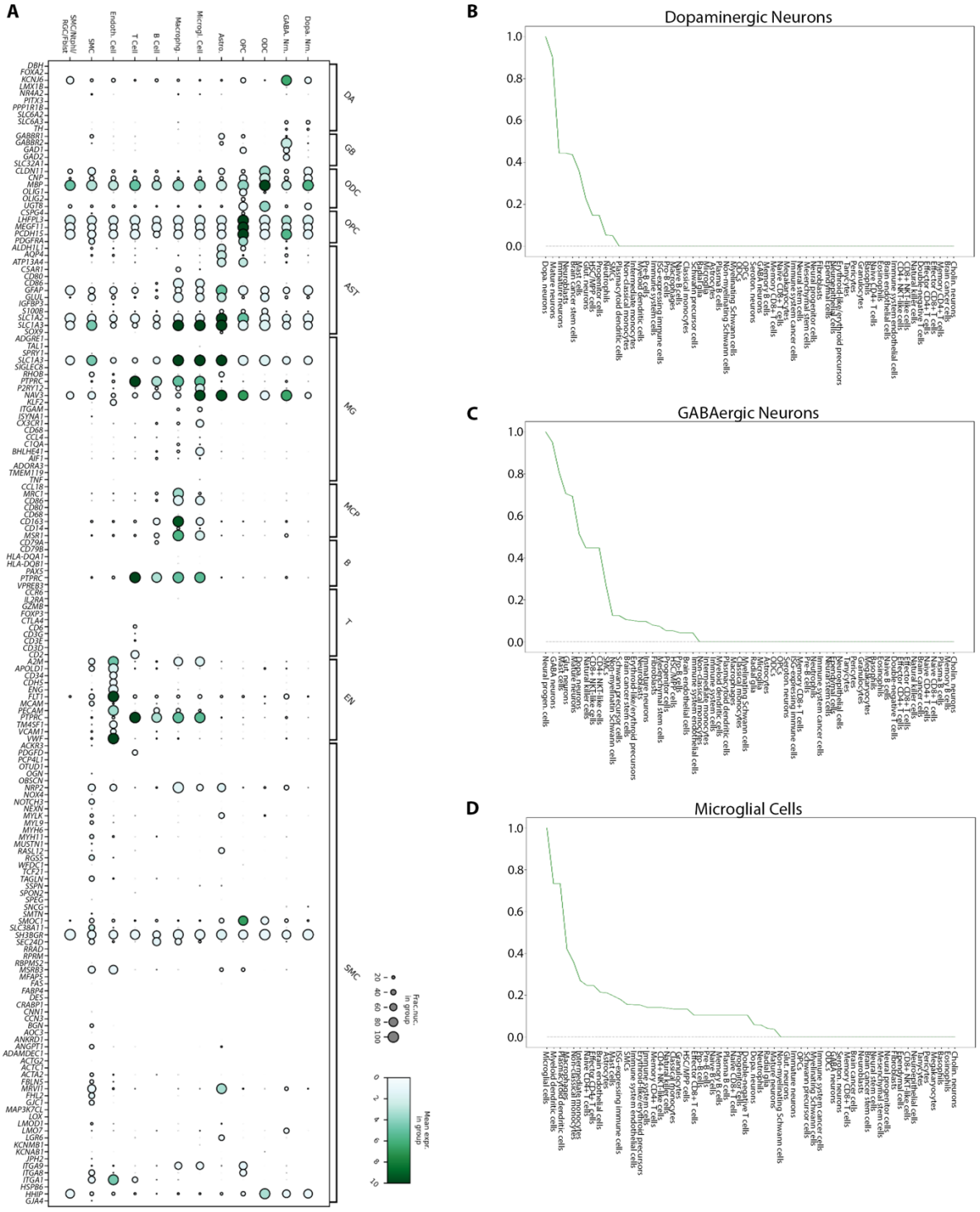

Fig. S5. Further information about likelihood-based cell typing of clusters.

(A) Dot plot showing, for each cell type in our dataset (top labels), expression of various expected SN cell type marker genes (left labels: expected marker genes, right labels: expected SN cell types). **(B)-(D)** Possible database (Data S6) cell types, ordered left to right by decreasing log-likelihood (and normalized to a maximum value of 1), for our **(B)** DA neuron, **(C)** GABA neuron, and **(D)** microglia clusters.

1540 **Table S1. (separate file)**
1541 Donor characteristics.
1542
1543 **Table S2. (separate file)**
1544 Statistical comparisons of donor characteristics across donor groups. Bold text with asterisks
1545 indicates $p<0.05$. Double dashes indicate repeated comparisons or not-relevant self-comparisons.
1546
1547 **Table S3.**
1548 Numbers of donors and nuclei per SUD drug class, by HIV status.

1549 **Table S4. (separate file)**
1550 snRNA-seq nuclear yields by donor and cell type.

1551 **Table S5. (separate file)**
1552 Statistical comparisons of cell type proportions across donor groups. Multiple-comparison-
1553 adjusted p-values are shown for Kolmogorov-Smirnov tests; bold and asterisks indicate $p<0.05$.
1554 The cell type proportions per donor group used in these comparisons are shown below this table.
1555
1556 **Table S6.**
1557 DA neuron (DA)/microglia (MG) DEG subcluster compositions, for SUD+/HIV+u DEAs.
1558
1559 **Table S7. (separate file)**
1560 Comparison of gene set enrichment results produced using Enrichr vs. GSEApy.
1561
1562 **Table S8.**
1563 Fractions of significantly correlated DEG pairs in subclustering analyses.
1564
1565

1566 **Table S3. Numbers of donors and nuclei per SUD drug class, by HIV status.**

HIV status	N donors N nuclei cocaine SUD	N donors N nuclei opioid SUD	N donors N nuclei cocaine + opioid SUDs	N donors N nuclei neither SUD	Total N for HIV status
HIV-	1 2,083	4 5,421	10 28,610	13 27,349	28 63,463
HIV+u	6 16,593	4 10,607	10 23,281	10 21,683	30 72,164
HIV+d	11 20,867	6 19,229	8 15,333	7 9,676	32 65,105
Total N for SUD drug class	18 39,543	14 35,257	28 67,224	30 58,708	90 200,732

1567
1568

1569 **Table S6. DA neuron (DA)/microglia (MG) DEG subcluster compositions, for SUD+/HIV+u**
1570 **DEAs.**

DEA (effect)	Total N DEG subclusters	Median (IQR) N DEGs per subcluster	Median (IQR) subcluster mean similarity	N mixed DA/MG DEG subclusters	Median (IQR) N DEGs per mixed DA/MG subcluster	Median (IQR) mixed DA/MG subcluster mean similarity
SUD+HIV- vs. SUD-HIV- **(SUD impacts without HIV)**	28	13 (7, 23)	0.88 (0.83, 0.94)	2	24 (20, 27)	0.91 (0.91, 0.92)
SUD-HIV+u vs. SUD-HIV- **(HIV+u impacts without SUD)**	34	8 (5, 20)	0.94 (0.89, 0.95)	6	10 (7, 14)	0.90 (0.87, 0.92)
SUD+HIV+u vs. SUD-HIV+u **(SUD impacts with HIV+u)**	28	12 (7, 21)	0.89 (0.85, 0.92)	6	16 (8, 38)	0.87 (0.80, 0.91)
SUD+HIV+u vs. SUD+HIV- **(HIV+u impacts with SUD)**	27	9 (5, 22)	0.89 (0.85, 0.92)	3	9 (7, 23)	0.90 (0.87, 0.91)
All	117	10 (6, 21)	0.91 (0.86, 0.95)	17	12 (6, 20)	0.90 (0.86, 0.92)

1571
1572
1573

1574 **Table S8. Fractions of significantly correlated DEG pairs in subclustering analyses.**

Cell type mix	N DEAs analyzed	Median (IQR) fraction significantly correlated DEG pairs per DEA, across DEAs
DA neurons, microglia	4	0.30 (0.28, 0.30)
GABA neurons, microglia	2	0.27 (0.27, 0.28)
DA neurons, GABA neurons	2	0.46 (0.44, 0.49)
All	8	0.30 (0.28, 0.34)

1575
1576

Data S1. (separate file)

DEG lists, organized by cell type (DA neuron, GABA neuron, or microglia) and DEA type (impacts of HIV or SUD).

Data S2. (separate file)

Lists of Enrichr gene sets enriched by DEGs per DEA, cell type, and direction of dysregulation (up/down). Significantly enriched gene sets (with adjusted p-value <0.05; column E) are highlighted in green.

Data S3. (separate file)

Basic annotations for DEG subclusters, organized by cell type.

Data S4. (separate file)

Focused annotations for DEG subclusters, with references.

Data S5. (separate file)

UMAPs comparing expression data before (left) vs. after (right) batch correction, showing nuclei from one donor across pooled libraries ("batches"). Each plot title lists the donor's ID, and each library is shown in a different color.

Data S6. (separate file)

Cell type marker gene database used for cell typing.

Data S7. (separate file)

Heatmaps of DEG subclusters showing significant DEG pairwise Pearson correlations and related underlying data.

Data S8. (separate file)

Heatmaps showing mean normalized counts for each subcluster's DEGs, per case group donor, with donors labeled by SUD drug class (opioid, cocaine, or opioid+cocaine) and organized by their cross-DEG expression similarities (shown with a dendrogram above each heatmap).

Data S9. (separate file)

Zip file containing lists of GSEApy prerank gene sets enriched by each DEA's DEGs, organized by cell type. Files with names ending in "__all" include all gene sets having any DEGs; files ending with "__sig" include only significantly enriched gene sets.

1608 **References**

1609

1610 1. Subramanian, A., Alperovich, M., Yang, Y. & Li, B. Biology-inspired data-driven quality

1611 control for scientific discovery in single-cell transcriptomics. *Genome Biol.* **23**, 267 (2022).

1612 2. Wei, J. *et al.* Single nucleus transcriptomics of ventral midbrain identifies glial activation

1613 associated with chronic opioid use disorder. *Nat. Commun.* **14**, 5610 (2023).

1614